Journal of Computational Physics 497 (2024) 112590

Contents lists available at ScienceDirect

Journal of Computational Physics

journal homepage: www.elsevier.com/locate/jcp

Two-step multi-resolution reconstruction-based compact gas-kinetic scheme on tetrahedral mesh

Xing Ji [a], Fengxiang Zhao [b,c], Wei Shyy [d], Kun Xu [b,c,d,e,*]

[a] State Key Laboratory for Strength and Vibration of Mechanical Structures, Shaanxi Key Laboratory of Environment and Control for Flight Vehicle, School of Aerospace Engineering, Xi'an Jiaotong University, Xi'an, China
[b] Department of Mathematics, Hong Kong University of Science and Technology, Clear Water Bay, Kowloon, Hong Kong
[c] Center for Ocean Research in Hong Kong and Macau (CORE), Hong Kong University of Science and Technology, Clear Water Bay, Kowloon, Hong Kong
[d] Department of Mechanical and Aerospace Engineering, Hong Kong University of Science and Technology, Clear Water Bay, Kowloon, Hong Kong
[e] Shenzhen Research Institute, Hong Kong University of Science and Technology, Shenzhen, China

ARTICLE INFO

Keywords:
Compact gas-kinetic scheme
Two-step reconstruction
Multi-resolution WENO
Two-stage time discretization
Navier-Stokes solution

ABSTRACT

This paper presents the development of a third-order compact gas-kinetic scheme (GKS) for compressible Euler and Navier-Stokes solutions, constructed particularly for an unstructured tetrahedral mesh. The scheme utilizes a time-dependent gas distribution function at a cell interface to not only calculate the fluxes needed for updating the cell-averaged flow variables but also to evaluate the flow variables at the cell interface. This leads to the evolution of cell-averaged gradients of flow variables. The success of this scheme heavily relies on the initial data reconstruction techniques, with an emphasis on their application to the tetrahedral mesh. Employing a conventional second-order unlimited least-square reconstruction directly on the cell-averaged flow variables of von Neumann neighbouring cells can introduce linear instability into the scheme. However, by using the updated cell-averaged gradients, the GKS with a third-order compact smooth reconstruction remains linearly stable under a large CFL number when applied to a tetrahedral mesh. To enhance the robustness of the high-order compact GKS for capturing a discontinuous solution, we propose a novel two-step multi-resolution weighted essentially non-oscillatory (WENO) reconstruction. This innovative approach overcomes the stability issues associated with a second-order compact reconstruction by incorporating a pre-reconstruction step. Additionally, it simplifies the third-order non-linear reconstruction process by adding a single large stencil to those used in the second-order one. A high-order wall boundary condition is achieved by fusing the constrained least-square technique with the WENO procedure, where a quadratic element is used in the reconstruction for cells with a curved boundary. Numerical tests involving both the second-order and third-order compact GKS are presented, encompassing both inviscid and viscous flows at both low and high speeds. The results demonstrate that the proposed third-order compact scheme possesses robustness in high-speed flow computation and exhibits excellent adaptability to meshes with complex geometrical configurations.

* Corresponding author at: Department of Mathematics, Hong Kong University of Science and Technology, Clear Water Bay, Kowloon, Hong Kong.
E-mail addresses: xjiad@connect.ust.hk (X. Ji), fzhaoac@connect.ust.hk (F. Zhao), weishyy@ust.hk (W. Shyy), makxu@ust.hk (K. Xu).

https://doi.org/10.1016/j.jcp.2023.112590
Received 12 February 2021; Received in revised form 16 September 2023; Accepted 19 October 2023

Available online 28 October 2023

1. Introduction

The simulation of compressible flow with complex geometry is important in the engineering applications. The use of unstructured mesh is especially favored from its geometric flexibility. On such a mesh even for a second-order finite volume method (FVM) it is not easy to achieve the same performance as that in the structured mesh. Commonly, slope reconstruction schemes, such as cell-based Green-Gauss method [16] combined with different types of limiters, are robust and widely used in the commercial or open-source software [38]. However, these methods can easily deteriorate the spatial accuracy for skewed mesh and become over-dissipative for flow simulation with discontinuities. The least-square reconstruction with cell-averaged variables and von Neumann neighbors only preserves a strictly second-order accuracy, but suffers from the linear instability on tetrahedral mesh [5]. Therefore, the reconstruction stencil has to be further extended. In order to ensure linear stability, a two-step second-order weighted essentially non-oscillatory (WENO) method has been proposed [31] with the attempt of keeping a compact reconstruction even with an extended stencil. The high-order WENO-FVMs have been continuously developed and applied to large-scale aeronautical simulations [1]. But, the compactness can be hardly kept in the high-order FVMs. Even though the extended stencils in reconstruction can improve the robustness of the schemes, difficulties still exist in the parallel programming and boundary treatment. The recently proposed multi-resolution reconstruction with only five equivalent sub-stencils greatly releases the above problems [39] even with the inclusion of neighbor-to-neighbor cells.

The compact methods with the updates of multiple degrees of freedom (DOFs) for each cell have been developed extensively in the past decades. Two main representatives are the DG [25] and the FR/CPR methods [6,35], which hybridize the finite volume framework with the finite element method or the finite difference method. These methods can achieve arbitrary spatial order of accuracy with only the targeted cell as the reconstruction stencil, and yield great mesh adaptability and high scalability. Successful examples have been demonstrated in large eddy simulation (LES) [29] and RANS simulation [34] for subsonic flows. For the flow simulation with discontinuities, these methods have less robustness against the traditional high-order FVMs. In addition, these methods have restricted explicit time steps and high memory-consumption [15]. The $P_N P_M$ [4] and reconstructed-DG (rDG) methods [15] try to overcome the above weakness with the release of the compactness of the DG methods. Large time step and less memory requirement can be achieved in the rDG methods in comparison with the same order DG ones.

In recent years, a class of high-order compact GKS (CGKS) has been developed. The GKS is based on a time accurate evolution model in the construction of the gas distribution function at a cell interface [33]. The time-dependent solution provides not only the fluxes across a cell interface, but also the corresponding flow variables. As a result, both the cell-averaged flow variables and their gradients can be updated simultaneously through the divergence theorem. For the DG/rDG methods, the similar DOFs are obtained differently with explicit governing equations. Due to their differences in the updating schemes, the compact GKS can use a larger time step and has better robustness than the corresponding DG methods. For example, a CFL number around 0.5 can be taken for the third-order compact GKS [9] while it is restricted to be less than 0.33 for the third-order P1P2-rDG scheme. The P1P2-rDG is claimed to be unstable on tetrahedral mesh with smooth reconstruction. However, as shown in this paper the third-order compact GKS is stable with a CFL number of 1 with the same compact stencil. Due to the use of time accurate evolution model, another advantage of GKS is to use the two-stage fourth-order temporal discretization method [12] or other multi-stage multi-derivative time marching scheme [23]. Although the gas-kinetic flux function has a high computational cost than the time-independent Riemann solvers, the HGKS can achieve fourth-order temporal accuracy with only two stages [19], instead of four-stages in the fourth-order Runge-Kutta (RK) time discretization. Overall, the compact GKS turns out to be more efficient in comparison with Riemann-solver-based RK methods [10,9].

In this paper, a compact third-order GKS on tetrahedral mesh will be presented. The scheme is linearly stable for smooth flow with unlimited constrained-least-square reconstruction on a compact stencil with von Neumann neighboring cells only. A direct application of the HWENO-type reconstruction on the hexahedral mesh [10] and on the current tetrahedron mesh is not successful, and shows poor robustness and mesh adaptability. The main reasons may be the following. Firstly, the coefficient matrices for the first-order polynomials obtained from the cell-averaged conservative variables on the biased sub-stencils depend too sensitively on the quality of the tetrahedron and can easily become singular. Secondly, the central first-order sub-stencil cannot provide a proper measurement of the smoothness of the local flow field. In the FVM, the unlimited second-order least-square reconstruction on such a central stencil leads to linear instability [5], same to the second-order GKS with the same reconstruction. Extended stencils have to be used to ensure the stability under finite volume framework. Recently, a two-step WENO reconstruction with a compact stencil in each step has been proposed [31]. The key idea is to firstly reconstruct the first-order spatial derivatives by using the unlimited least-square reconstruction and store them in each cell. Then, at the second step, new first-order spatial derivatives on the targeting cell are obtained by a weighted combination of all the pre-computed spatial derivatives. At the same time, a multi-resolution reconstruction has been proposed in a hierarchical way, i.e., the Nth-order of accuracy can be achieved by N central stencils from first-order to Nth-order [39]. Inspired from the above two approaches, a two-step multi-resolution reconstruction is designed in the current scheme. A linearly stable second-order WENO reconstruction is obtained first in a compact manner. Then, a third-order compact reconstruction is obtained with one additional large stencil only beside the above second-order one. The reconstruction becomes simple and efficient. For example, the robustness and mesh adaptability of the scheme have been enhanced due to the extended sub-stencils, and the memory overhead is even sightly reduced without storing the polynomial coefficients of the biased sub-stencils in each cell. Benefiting from the compact reconstruction in each step, the WENO procedure can be easily extended to the boundary reconstruction. In order to keep high-order accuracy at boundaries, a third-order one-sided reconstruction without ghost cells are designed for the adiabatic and isothermal walls at each Gaussian point. To keep the high-order spatial reconstruction, a quadratic

element is used to recover the curved boundary. Stringent tests including supersonic flow passing through an air-vehicle validate the robustness of the current compact scheme with complex geometry.

This paper is organized as follows. The basic framework of the compact high-order GKS on tetrahedron mesh is presented in Section 2. In Section 3, the basic formulation for the two-stage temporal discretization is given. In Section 4, the details for the two-step multi-resolution WENO reconstruction on tetrahedral mesh are presented. Numerical examples from nearly incompressible to highly compressible flows are shown in Section 5. A concluding remark is drawn in the last section.

2. Compact finite volume gas-kinetic scheme

The 3-D gas-kinetic BGK equation [2] is

$$f_t + \mathbf{u}\cdot\nabla f = \frac{g-f}{\tau}, \tag{1}$$

where $f = f(\mathbf{x}, t, \mathbf{u}, \xi)$ is the gas distribution function, which is a function of space $\mathbf{x}$, time t, particle velocity $\mathbf{u}$, and internal variable ξ. g is the equilibrium state approached by f and τ is the collision time.

The collision term satisfies the compatibility condition

$$\int \frac{g-f}{\tau}\boldsymbol{\psi}\mathrm{d}\Xi = 0, \tag{2}$$

where $\boldsymbol{\psi} = (1, \mathbf{u}, \frac{1}{2}(\mathbf{u}^2+\xi^2))^T$, $\mathrm{d}\Xi = \mathrm{d}u_1\mathrm{d}u_2\mathrm{d}u_3\mathrm{d}\xi_1\ldots\mathrm{d}\xi_K$, K is the number of internal degrees of freedom, i.e. $K = (5-3\gamma)/(\gamma-1)$ in 3-D case, and γ is the specific heat ratio.

In the continuum flow regime with the smoothness assumption, based on the Chapman-Enskog expansion of the BGK equation the gas distribution function can be expressed as [33],

$$f = g - \tau D_{\mathbf{u}} g + \tau D_{\mathbf{u}}(\tau D_{\mathbf{u}})g - \tau D_{\mathbf{u}}[\tau D_{\mathbf{u}}(\tau D_{\mathbf{u}})g] + \ldots,$$

where $D_{\mathbf{u}} = \partial/\partial t + \mathbf{u}\cdot\nabla$. Different hydrodynamic equations can be derived by truncating the expansion on different orders of τ. With the zeroth-order in truncated distribution function $f = g$, the Euler equations can be recovered by multiplying $\boldsymbol{\psi}$ on Eq. (1) and integrating it over the phase space,

$$\mathbf{W}_t + \nabla\cdot\mathbf{F}(\mathbf{W}) = 0.$$

With the first-order truncation, i.e.,

$$f = g - \tau(\mathbf{u}\cdot\nabla g + g_t), \tag{3}$$

the N-S equations can be obtained,

$$\mathbf{W}_t + \nabla\cdot\mathbf{F}(\mathbf{W}, \nabla\mathbf{W}) = 0,$$

with $\tau = \mu/p$ and $Pr = 1$.

The conservative variables and their fluxes are the moments of the gas distribution function

$$\mathbf{W}(\mathbf{x}, t) = \int \boldsymbol{\psi} f(\mathbf{x}, t, \mathbf{u}, \xi)\mathrm{d}\Xi \tag{4}$$

and

$$\mathbf{F}(\mathbf{x}, t) = \int \mathbf{u}\boldsymbol{\psi} f(\mathbf{x}, t, \mathbf{u}, \xi)\mathrm{d}\Xi. \tag{5}$$

Remark 1. The cell-averaged conservative variables can be updated through the interface fluxes under the finite volume framework. Besides the fluxes in Eq. (5), the gas distribution function also provides the flow variables at the cell interface, such as that in Eq. (4). It is the key point for the construction of compact GKS with the availability of time accurate $\mathbf{W}(\mathbf{x}, t)$ at a cell interface. The scheme depends solely on the high-order gas evolution model for providing local time accurate evolution solution, which cannot be achieved by time independent Riemann solution.

2.1. Compact gas-kinetic scheme on tetrahedral mesh

For a tetrahedral cell Ω_i in 3-D case, the boundary can be expressed as

$$\partial\Omega_i = \bigcup_{p=1}^{N_f}\Gamma_{ip},$$

where $N_f = 4$ is the number of cell interfaces for cell Ω_i.

The update of the cell averaged conservative flow variables in a finite control volume i from t_n to t_{n+1} can be expressed as

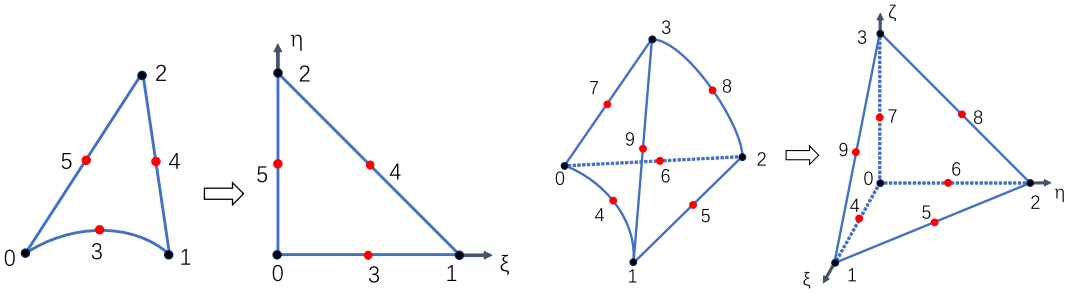

(a) Quadratic triangluar surface (b) Quadratic tetrahedral volume

Fig. 1. The controlling points and isoparametric transformation of the quadratic elements.

$$\mathbf{W}_i^{n+1}\left|\Omega_i\right| = \mathbf{W}_i^{n}\left|\Omega_i\right| - \sum_{p=1}^{N_f}\int_{\Gamma_{ip}}\int_{t_n}^{t_{n+1}} \mathbf{F}(\mathbf{x},t)\cdot\mathbf{n}_p \mathrm{d}t\mathrm{d}s, \tag{6}$$

with

$$\mathbf{F}(\mathbf{x},t)\cdot\mathbf{n}_p = \int \boldsymbol{\psi} f(\mathbf{x},t,\mathbf{u},\xi)\mathbf{u}\cdot\mathbf{n}_p \mathrm{d}\Xi, \tag{7}$$

where $\mathbf{W}_i$ is the cell averaged values over cell Ω_i, $\left|\Omega_i\right|$ is the volume of Ω_i, $\mathbf{F}$ is the interface fluxes, and $\mathbf{n}_p = (n_1, n_2, n_3)^T$ is the unit vector in the outer normal direction of Γ_{ip}. The semi-discretized form of finite volume scheme can be written as

$$\frac{\mathrm{d}\mathbf{W}_i}{\mathrm{d}t} = \mathcal{L}(\mathbf{W}_i) = -\frac{1}{\left|\Omega_i\right|}\sum_{p=1}^{N_f}\int_{\Gamma_{ip}} \mathbf{F}(\mathbf{W})\cdot\mathbf{n}_p \mathrm{d}s. \tag{8}$$

For the interface fluxes $\mathbf{F}_{ip}(t)$, the numerical quadrature can be adopted and Eq. (6) can be rewritten as

$$\mathbf{W}_i^{n+1}\left|\Omega_i\right| = \mathbf{W}_i^{n}\left|\Omega_i\right| - \sum_{p=1}^{N_f}\left|\Gamma_{ip}\right|\sum_{k=1}^{M}\omega_k\int_{t_n}^{t_{n+1}} \mathbf{F}(\mathbf{x}_{p,k},t)\cdot\mathbf{n}_p \mathrm{d}t. \tag{9}$$

Nowadays the curved mesh generation has been supported by popular commercial software. To be consistent with the spatial accuracy, the quadratic element is applied here to describe the geometry. The controlling points for the quadratic triangle are shown in Fig. 1(a). The iso-parametric transformation is used to evaluate the surface integral, which is expressed as

$$\mathbf{X}(\xi,\eta) = \sum_{l=0}^{5}\mathbf{x}_l\phi_l(\xi,\eta),$$

where $\mathbf{x}_l$ is the location of the controlling points and ϕ_l is the base function as follows [28]

$$\begin{aligned} &\phi_0 = (\xi+\eta-1)(2\xi+2\eta-1), \quad \phi_1 = \xi(2\xi-1), \quad \phi_2 = \eta(2\eta-1),\\ &\phi_3 = -4\xi(\xi+\eta-1), \quad \phi_4 = 4\xi\eta, \quad \phi_5 = -4\eta(\xi+\eta-1). \end{aligned} \tag{10}$$

The flux across Γ_{ip} in Eq. (6) can be transferred to a standard isosceles right triangle $\tilde{\Gamma}_{ip}$

$$\mathbf{F}_{ip}(t) = \int_{\Gamma_{ip}} \mathbf{F}(\mathbf{x},t)\cdot\mathbf{n}_p \mathrm{d}s = \int_{\tilde{\Gamma}_{ip}} \mathbf{F}(\mathbf{W}(\mathbf{X}(\xi,\eta)))\cdot\mathbf{n}_p \left|\frac{\partial(x,y,z)}{\partial(\xi,\eta)}\right| \mathrm{d}\xi\mathrm{d}\eta.$$

To meet the requirement of a third-order spatial accuracy, the above equation can be approximated through Gaussian quadrature as

$$\mathbf{F}_{ip}(t) = \frac{1}{2}\Delta\xi\Delta\eta\sum_{m=1}^{3}\tilde{\omega}_m\mathbf{F}_m(t)\cdot(\mathbf{n}_p)_m\left|\frac{\partial(x,y,z)}{\partial(\xi,\eta)}\right|_m,$$

where $\Delta\xi = \Delta\eta = 1$ and the local normal direction $(\mathbf{n}_p)_m = \left(\boldsymbol{X}_\xi \times \boldsymbol{X}_\eta\right) / \left\|\boldsymbol{X}_\xi \times \boldsymbol{X}_\eta\right\|$. The standard Gaussian points are

$$(\xi,\eta)_1 = (\frac{1}{6}\Delta\xi, \frac{1}{6}\Delta\eta),\ (\xi,\eta)_2 = (\frac{2}{3}\Delta\xi, \frac{1}{6}\Delta\eta),\ (\xi,\eta)_3 = (\frac{1}{6}\Delta\xi, \frac{2}{3}\Delta\eta),$$

with $\tilde{\omega}_m = \frac{1}{3}$, $m = 1,2,3$. Compared with Eq. (9), we have

$$\omega_m = \frac{1}{2}\tilde{\omega}_m\left|\frac{\partial(x,y,z)}{\partial(\xi,\eta)}\right|_m,\ \mathbf{x}_{p,k} = \mathbf{x}((\xi,\eta))_m,\ \mathbf{n}_{p,k} = (\mathbf{n}_p)_m,\quad m = 1,2,3.$$

The quadratic element reduces to the linear element when every edge is a straight line.

According to the coordinate transformation, the local coordinate for the cell interface Γ_{ip} is expressed as $(\widetilde{x}_1, \widetilde{x}_2, \widetilde{x}_3)^T = (0, \widetilde{x}_2, \widetilde{x}_3)^T$, where $(\widetilde{x}_2, \widetilde{x}_3)^T \in \Gamma_{ip}$, and the velocities in the local coordinate are given by

$$\begin{cases} \tilde{u}_1 = u_1 n_1 + u_2 n_2 + u_3 n_3, \\ \tilde{u}_2 = -u_1 n_2 + u_2 (n_1 + \frac{n_3^2}{1+n_1}) - u_3 \frac{n_2 n_3}{1+n_1}, \quad n_1 \neq -1. \\ \tilde{u}_3 = -u_1 n_3 - u_2 \frac{n_2 n_3}{1+n_1} + u_3 (1 - \frac{n_3^2}{1+n_1}), \end{cases} \tag{11}$$

The macroscopic conservative flow variables in the local coordinate are expressed as

$$\widetilde{\mathbf{W}}(\widetilde{\mathbf{x}}, t) = \mathbf{T}\mathbf{W}(\mathbf{x}, t),$$

where $\mathbf{T}$ is the rotation matrix

$$\mathbf{T} = \begin{pmatrix} 1 & 0 & 0 & 0 & 0 \\ 0 & n_1 & n_2 & n_3 & 0 \\ 0 & -n_2 & n_1 + \frac{n_3^2}{1+n_1} & -\frac{n_2 n_3}{1+n_1} & 0 \\ 0 & -n_3 & -\frac{n_2 n_3}{1+n_1} & 1 - \frac{n_3^2}{1+n_1} & 0 \\ 0 & 0 & 0 & 0 & 1 \end{pmatrix}, \quad n_1 \neq -1. \tag{12}$$

Note that when $n_1 = -1$, Eq. (11) changes to $(\tilde{u}_1, \tilde{u}_2, \tilde{u}_3)^T = (-u_1, -u_2, u_3)^T$ and the matrix (12) is replaced by a diagonal matrix $\Lambda = \mathrm{diag}(1, -1, -1, 1, 1)$.

For the gas distribution function in the local coordinate, $\widetilde{f}(\widetilde{\mathbf{x}}, t, \widetilde{\mathbf{u}}, \xi) = f(\mathbf{x}, t, \mathbf{u}, \xi)$ and $|\mathrm{d}\mathbf{u}| = |\mathrm{d}\widetilde{\mathbf{u}}|$, then the numerical fluxes can be transformed as

$$\mathbf{F}(\mathbf{x}, t) = \int \boldsymbol{\psi} f(\mathbf{x}, t, \mathbf{u}, \xi) \mathbf{u} \cdot \mathbf{n}_p \mathrm{d}\mathbf{u}\mathrm{d}\xi = \int \boldsymbol{\psi} \widetilde{f}(\widetilde{\mathbf{x}}, t, \widetilde{\mathbf{u}}, \xi) \widetilde{u}_1 \mathrm{d}\widetilde{\mathbf{u}}\mathrm{d}\xi. \tag{13}$$

In the computation, the fluxes are obtained firstly by taking moments of the gas distribution function in the local coordinates

$$\widetilde{\mathbf{F}}(\widetilde{\mathbf{x}}, t) = \int \widetilde{\boldsymbol{\psi}} \widetilde{f}(\widetilde{\mathbf{x}}, t, \widetilde{\mathbf{u}}, \xi) \widetilde{u}_1 \mathrm{d}\widetilde{\mathbf{u}}\mathrm{d}\xi, \tag{14}$$

where $\widetilde{\boldsymbol{\psi}} = (1, \widetilde{\mathbf{u}}, \frac{1}{2}(\widetilde{\mathbf{u}}^2 + \xi^2))^T$. According to Eq. (11), Eq. (13) and Eq. (14), the fluxes in the global coordinate can be expressed as a combination of the fluxes in the local coordinate

$$\mathbf{F}(\mathbf{W}(\mathbf{x}, t)) \cdot \mathbf{n} = \mathbf{T}^{-1} \widetilde{\mathbf{F}}(\widetilde{\mathbf{W}}(\widetilde{\mathbf{x}}, t)). \tag{15}$$

2.2. Gas-kinetic solver

In order to construct the numerical fluxes at $\mathbf{x} = (0, 0, 0)^T$, the integral solution of BGK equation Eq. (1) is used

$$f(\mathbf{x}, t, \mathbf{u}, \xi) = \frac{1}{\tau} \int_0^t g(\mathbf{x}', t', \mathbf{u}, \xi) e^{-(t-t')/\tau} \mathrm{d}t' + e^{-t/\tau} f_0(\mathbf{x} - \mathbf{u}t, \mathbf{u}, \xi), \tag{16}$$

where $\mathbf{x} = \mathbf{x}' + \mathbf{u}(t - t')$ is the particle trajectory. f_0 is the initial gas distribution function, g is the corresponding equilibrium state in space and time. The integral solution basically states a physical process from the particle free transport of f_0 in the kinetic scale to the hydrodynamic flow evolution in the integration of g term. The flow evolution at the cell interface depends on the ratio of time step to the local particle collision time $\Delta t/\tau$.

To construct a time evolving gas distribution function at a cell interface, the following notations are introduced first

$$a_{x_i} \equiv (\partial g/\partial x_i)/g = g_{x_i}/g, A \equiv (\partial g/\partial t)/g = g_t/g,$$

where g is the equilibrium state. The variables (a_{x_i}, A), denoted by s, depend on particle velocity in the form of [32]

$$s = s_j \psi_j = s_1 + s_2 u_1 + s_3 u_2 + s_4 u_3 + s_5 \frac{1}{2}(u_1^2 + u_2^2 + u_3^2 + \xi^2).$$

The initial gas distribution function in the solution (16) can be modeled as

$$f_0 = f_0^l(\mathbf{x}, \mathbf{u}) \mathbb{H}(x_1) + f_0^r(\mathbf{x}, \mathbf{u})(1 - \mathbb{H}(x_1)),$$

where $\mathbb{H}(x_1)$ is the Heaviside function. Here f_0^l and f_0^r are the initial gas distribution functions on both sides of a cell interface, which have one to one correspondence with the initially reconstructed macroscopic variables. The first-order Taylor expansion for the gas distribution function in space around $\mathbf{x} = \mathbf{0}$ can be expressed as

$$f_0^k(\mathbf{x}) = f_G^k(\mathbf{0}) + \frac{\partial f_G^k}{\partial x_i}(\mathbf{0})x_i = f_G^k(\mathbf{0}) + \frac{\partial f_G^k}{\partial x_1}(\mathbf{0})x_1 + \frac{\partial f_G^k}{\partial x_2}(\mathbf{0})x_2 + \frac{\partial f_G^k}{\partial x_3}(\mathbf{0})x_3, \tag{17}$$

for $k = l, r$. According to Eq. (3), f_G^k has the form

$$f_G^k(\mathbf{0}) = g^k(\mathbf{0}) - \tau(u_i g_{x_i}^k(\mathbf{0}) + g_t^k(\mathbf{0})), \tag{18}$$

where g^k is the equilibrium state with the form of a Maxwell distribution. g^k can be fully determined from the reconstructed macroscopic variables $\mathbf{W}^l, \mathbf{W}^r$ at the left and right sides of a cell interface

$$\int \boldsymbol{\psi} g^l \mathrm{d}\Xi = \mathbf{W}^l, \int \boldsymbol{\psi} g^r \mathrm{d}\Xi = \mathbf{W}^r. \tag{19}$$

Substituting Eq. (17) and Eq. (18) into Eq. (16), the kinetic part of the integral solution can be written as

$$e^{-t/\tau} f_0^k(-\mathbf{u}t, \mathbf{u}, \xi) = e^{-t/\tau} g^k[1 - \tau(a_{x_i}^k u_i + A^k) - t a_{x_i}^k u_i], \tag{20}$$

where the coefficients $a_{x_1}^k, ..., A^k, k = l, r$ are defined according to the expansion of g^k. After determining the kinetic part f_0, the equilibrium state g in the integral solution Eq. (16) can be expanded in space and time as follows

$$g(\mathbf{x}, t) = g^c(\mathbf{0}, 0) + \frac{\partial g^c}{\partial x_i}(\mathbf{0}, 0)x_i + \frac{\partial g^c}{\partial t}(\mathbf{0}, 0)t, \tag{21}$$

where g^c is the Maxwellian equilibrium state located at an interface. Similarly, $\mathbf{W}^c$ are the macroscopic flow variables for the determination of the equilibrium state g^c

$$\int \boldsymbol{\psi} g^c \mathrm{d}\Xi = \mathbf{W}^c. \tag{22}$$

Substituting Eq. (21) into Eq. (16), the hydrodynamic part in the integral solution can be written as

$$\frac{1}{\tau}\int_0^t g(\mathbf{x}', t', \mathbf{u}, \xi) e^{-(t-t')/\tau} \mathrm{d}t' = C_1 g^c + C_2 a_{x_i}^c u_i g^c + C_3 A^c g^c, \tag{23}$$

where the coefficients $a_{x_i}^c, A^c$ are defined from the expansion of the equilibrium state g^c. The coefficients $C_m, m = 1, 2, 3$ in Eq. (23) are given by

$$C_1 = 1 - e^{-t/\tau}, C_2 = (t + \tau)e^{-t/\tau} - \tau, C_3 = t - \tau + \tau e^{-t/\tau}.$$

The coefficients in Eq. (20) and Eq. (23) can be determined by the spatial derivatives of macroscopic flow variables and the compatibility condition as follows

$$\begin{aligned} &\langle a_{x_1} \rangle = \frac{\partial \mathbf{W}}{\partial x_1} = \mathbf{W}_{x_1}, \langle a_{x_2} \rangle = \frac{\partial \mathbf{W}}{\partial x_2} = \mathbf{W}_{x_2}, \langle a_{x_3} \rangle = \frac{\partial \mathbf{W}}{\partial x_3} = \mathbf{W}_{x_3}, \\ &\langle A + a_{x_1} u_1 + a_{x_2} u_2 + a_{x_3} u_3 \rangle = 0, \end{aligned} \tag{24}$$

where $\langle ... \rangle$ are the moments of a gas distribution function defined by

$$\langle (...) \rangle = \int \boldsymbol{\psi}(...) g \mathrm{d}\Xi. \tag{25}$$

The details for the evaluation of each term from macroscopic variables can be found in [7].

In smooth flow region, the collision time is determined by $\tau = \mu/p$, where μ is the dynamic viscosity coefficient and p is the pressure at the cell interface. In order to properly capture the un-resolved shock structure, additional numerical dissipation is needed. The physical collision time τ in the exponential function part can be replaced by a numerical collision time τ_n. For the inviscid flow, the collision time τ_n is modified as

$$\tau_n = \varepsilon \Delta t + C|\frac{p_l - p_r}{p_l + p_r}|\Delta t,$$

where $\varepsilon = 0.01$ and $C = 1$. For the viscous flow, the collision time is related to the viscosity coefficient,

$$\tau_n = \frac{\mu}{p} + C|\frac{p_l - p_r}{p_l + p_r}|\Delta t,$$

where p_l and p_r denote the pressure on the left and right sides of the cell interface. The inclusion of the pressure jump term is to increase the non-equilibrium transport mechanism in the flux function to mimic the physical process in the shock layer. Then substituting Eq. (20) and Eq. (23) into Eq. (16) with τ and τ_n, the final second-order time dependent gas distribution function becomes

$$f(\mathbf{0}, t, \mathbf{u}, \xi) = (1 - e^{-t/\tau_n})g^c + [(t + \tau)e^{-t/\tau_n} - \tau]a_{x_i}^c u_i g^c + (t - \tau + \tau e^{-t/\tau_n})A^c g^c$$

$$+e^{-t/\tau_n} g^l[1-(\tau+t)a^l_{x_i}u_i-\tau A^l]H(u_1)$$
$$+e^{-t/\tau_n} g^r[1-(\tau+t)a^r_{x_i}u_i-\tau A^r](1-H(u_1)). \tag{26}$$

For smooth flow, the time dependent solution in Eq. (26) can be simplified as [32],

$$f(\mathbf{0},t,\mathbf{u},\xi)=g^c-\tau(a^c_{x_i}u_i+A^c)g^c+A^c g^c t, \tag{27}$$

under the assumptions of $g^{l,r}=g^c$, $a^{l,r}_{x_i}=a^c_{x_i}$. The above gas-kinetic solver for smooth flow has less numerical dissipation than that from the full GKS solver in Eq. (26).

2.3. Direct evolution of the cell averaged first-order spatial derivatives

As shown in Eq. (26), a time evolution solution at a cell interface is provided by the gas-kinetic solver, which is distinguishable from the Riemann solver with a constant solution at a cell interface. Recall Eq. (4), the conservative variables at the Gaussian point $\mathbf{x}_{p,k}$ can be updated by taking moments $\boldsymbol{\psi}$ on the gas distribution function,

$$\mathbf{W}_{p,k}(t^{n+1})=\int \boldsymbol{\psi} f^n(\mathbf{x}_{p,k},t^{n+1},\mathbf{u},\xi)\mathrm{d}\Xi,\ k=1,...,M. \tag{28}$$

Then the cell-averaged first-order derivatives within each element at t^{n+1} is given through the Gauss's theorem,

$$\begin{aligned}
\overline{W}_x^{n+1}&=\frac{1}{\Delta V}\int_V \nabla\cdot(W(t^{n+1}),0,0)\mathrm{d}V=\frac{1}{\Delta V}\int_{\partial V}(1,0,0)\cdot\mathbf{n}W(t^{n+1})\mathrm{d}S\\
&=\frac{1}{\Delta V}\int_{\partial V}W(t^{n+1})n_1\mathrm{d}S=\frac{1}{\Delta V}\sum_{p=1}^{N_f}\sum_{k=1}^{M}\omega_{p,k}W^{n+1}_{p,k}(n_1)_{p,k}\Delta S_p,\\
\overline{W}_y^{n+1}&=\frac{1}{\Delta V}\int_V \nabla\cdot(0,W(t^{n+1}),0)\mathrm{d}V=\frac{1}{\Delta V}\int_{\partial V}(0,1,0)\cdot\mathbf{n}W(t^{n+1})\mathrm{d}S\\
&=\frac{1}{\Delta V}\int_{\partial V}W(t^{n+1})n_2\mathrm{d}S=\frac{1}{\Delta V}\sum_{p=1}^{N_f}\sum_{k=1}^{M}\omega_{p,k}W^{n+1}_{p,k}(n_2)_{p,k}\Delta S_p,\\
\overline{W}_z^{n+1}&=\frac{1}{\Delta V}\int_V \nabla\cdot(0,0,W(t^{n+1}))\mathrm{d}V=\frac{1}{\Delta V}\int_{\partial V}(0,0,1)\cdot\mathbf{n}W(t^{n+1})\mathrm{d}S\\
&=\frac{1}{\Delta V}\int_{\partial V}W(t^{n+1})n_3\mathrm{d}S=\frac{1}{\Delta V}\sum_{p=1}^{N_f}\sum_{k=1}^{M}\omega_{p,k}W^{n+1}_{p,k}(n_3)_{p,k}\Delta S_p,
\end{aligned} \tag{29}$$

where $\mathbf{n}_{p,k}=((n_1)_{p,k},(n_2)_{p,k},(n_3)_{p,k})$ is the outer unit normal direction at each Gaussian point $\mathbf{x}_{p,k}$.

3. Two-stage temporal discretization

The two-stage fourth-order (S2O4) temporal discretization is adopted here as that in the previous compact GKSs [9,36,10]. Following the definition of Eq. (8), a fourth-order time-accurate solution for the cell-averaged conservative flow variables $\mathbf{W}_i$ are updated by

$$\begin{aligned}
\mathbf{W}_i^*&=\mathbf{W}_i^n+\frac{1}{2}\Delta t\mathcal{L}(\mathbf{W}_i^n)+\frac{1}{8}\Delta t^2\frac{\partial}{\partial t}\mathcal{L}(\mathbf{W}_i^n),\\
\mathbf{W}_i^{n+1}&=\mathbf{W}_i^n+\Delta t\mathcal{L}(\mathbf{W}_i^n)+\frac{1}{6}\Delta t^2\Big(\frac{\partial}{\partial t}\mathcal{L}(\mathbf{W}_i^n)+2\frac{\partial}{\partial t}\mathcal{L}(\mathbf{W}_i^*)\Big),
\end{aligned} \tag{30}$$

where $\mathcal{L}(\mathbf{W}_i^n)$ and $\frac{\partial}{\partial t}\mathcal{L}(\mathbf{W}_i^n)$ are given by

$$\begin{aligned}
\mathcal{L}(\mathbf{W}_i^n)&=-\frac{1}{|\Omega_i|}\sum_{p=1}^{N_f}\sum_{k=1}^{M}\omega_{p,k}\mathbf{F}(\mathbf{x}_{p,k},t_n)\cdot\mathbf{n}_{p,k},\\
\frac{\partial}{\partial t}\mathcal{L}(\mathbf{W}_i^n)&=-\frac{1}{|\Omega_i|}\sum_{p=1}^{N_f}\sum_{k=1}^{M}\omega_{p,k}\partial_t\mathbf{F}(\mathbf{x}_{p,k},t_n)\cdot\mathbf{n}_{p,k},\\
\frac{\partial}{\partial t}\mathcal{L}(\mathbf{W}_i^*)&=-\frac{1}{|\Omega_i|}\sum_{p=1}^{N_f}\sum_{k=1}^{M}\omega_{p,k}\partial_t\mathbf{F}(\mathbf{x}_{p,k},t_*)\cdot\mathbf{n}_{p,k}.
\end{aligned} \tag{31}$$

The proof for the fourth-order accuracy in time is shown in [12].

In order to obtain the numerical fluxes $\mathbf{F}_{p,k}$ and their time derivatives $\partial_t \mathbf{F}_{p,k}$ at t_n and $t_* = t_n + \Delta t/2$, the time accurate solution in Eq. (26) can be approximated as a linear function of time. Let's first introduce the following notation,

$$\mathbb{F}_{p,k}(\mathbf{W}^n, \delta) = \int_{t_n}^{t_n+\delta} \mathbf{F}_{p,k}(\mathbf{W}^n, t)\mathrm{d}t.$$

For convenience, assume $t_n = 0$, the flux in the time interval $[t_n, t_n + \Delta t]$ is expanded in the linear form

$$\mathbf{F}_{p,k}(\mathbf{W}^n, t) = \mathbf{F}^n_{p,k} + t\partial_t \mathbf{F}^n_{p,k}.$$

The coefficients $\mathbf{F}^n_{p,k}$ and $\partial_t \mathbf{F}^n_{p,k}$ can be fully determined by

$$\begin{aligned}
&\mathbf{F}_{p,k}(\mathbf{W}^n, t_n)\Delta t + \frac{1}{2}\partial_t \mathbf{F}_{p,k}(\mathbf{W}^n, t_n)\Delta t^2 = \mathbb{F}_{p,k}(\mathbf{W}^n, \Delta t),\\
&\frac{1}{2}\mathbf{F}_{p,k}(\mathbf{W}^n, t_n)\Delta t + \frac{1}{8}\partial_t \mathbf{F}_{p,k}(\mathbf{W}^n, t_n)\Delta t^2 = \mathbb{F}_{p,k}(\mathbf{W}^n, \Delta t/2).
\end{aligned}$$

By solving the linear system, we have

$$\begin{aligned}
\mathbf{F}_{p,k}(\mathbf{W}^n, t_n) &= (4\mathbb{F}_{p,k}(\mathbf{W}^n, \Delta t/2) - \mathbb{F}_{p,k}(\mathbf{W}^n, \Delta t))/\Delta t,\\
\partial_t \mathbf{F}_{p,k}(\mathbf{W}^n, t_n) &= 4(\mathbb{F}_{p,k}(\mathbf{W}^n, \Delta t) - 2\mathbb{F}_{p,k}(\mathbf{W}^n, \Delta t/2))/\Delta t^2.
\end{aligned} \tag{32}$$

Finally, with Eq. (31) and (32), $\mathbf{W}_i^{n+1}$ at t^{n+1} can be updated by Eq. (30).

The time dependent gas distribution function at a cell interface is updated in a similar way,

$$\begin{aligned}
f^* &= f^n + \frac{1}{2}\Delta t f_t^n,\\
f^{n+1} &= f^n + \Delta t f_t^*.
\end{aligned} \tag{33}$$

In order to construct the first-order time derivative of the gas distribution function, the distribution function in Eq. (26) is approximated by the linear function

$$f(t) = f(\mathbf{x}_{p,k}, t, \mathbf{u}, \xi) = f^n + f_t^n(t - t^n).$$

According to the gas-distribution function at $t = 0$ and Δt

$$\begin{aligned}
f^n &= f(0),\\
f^n + f_t^n \Delta t &= f(\Delta t),
\end{aligned}$$

the coefficients f^n, f_t^n can be determined by

$$\begin{aligned}
f^n &= f(0),\\
f_t^n &= (f(\Delta t) - f(0))/\Delta t.
\end{aligned}$$

Thus, f^* and f^{n+1} are fully determined and the macroscopic flow variables at the cell interface can be obtained by Eq. (4). Theoretically, a fourth-order temporal accuracy can be achieved for the conservative flow variables on arbitrary mesh. The proof is given in [36].

4. Compact HWENO reconstruction

In this section, a compact HWENO-type reconstruction is designed to get the piecewise discontinuous flow variables and their first-order derivatives at each Gaussian point on both sides of a cell interface. The reconstruction procedure for an inner cell is given first, then the special treatment for the boundary cell is presented in subsequent section 4.4.

4.1. Smooth reconstruction

As a starting point of WENO reconstruction, a linear reconstruction will be presented first. For a piecewise smooth function $Q(\mathbf{x})$ over cell Ω_0, a polynomial $P^r(\mathbf{x})$ with degree r can be constructed to approximate $Q(\mathbf{x})$ as follows

$$P^r(\mathbf{x}) = Q(\mathbf{x}) + O(\Delta h^{r+1}),$$

where $\Delta h \sim |\Omega_0|^{\frac{1}{3}}$ is the equivalent cell size. In order to achieve a third-order accuracy and satisfy conservative property, the following quadratic polynomial over cell Ω_0 is obtained

$$P^2(\mathbf{x}) = \overline{Q}_0 + \sum_{|k|=1}^{2} a_k p^k(\mathbf{x}), \tag{34}$$

where $\overline{Q}_0$ is the cell averaged value of $Q(\mathbf{x})$ over cell Ω_0, $k=(k_1,k_2,k_3)$, $|k|=k_1+k_2+k_3$. The $p^k(\mathbf{x})$ are basis functions, which are given by

$$p^k(\mathbf{x})=x_1^{k_1}x_2^{k_2}x_3^{k_3}-\frac{1}{|\Omega_0|}\iiint_{\Omega_0}x_1^{k_1}x_2^{k_2}x_3^{k_3}\mathrm{d}V. \tag{35}$$

The controlling points for a quadratic tetrahedron are shown in Fig. 1(b). The iso-parametric transformation is used to evaluate the volume integral, which can be written as

$$\mathbf{X}(\xi,\eta,\zeta)=\sum_{i=0}^{9}\mathbf{x}_i\phi_i(\xi,\eta,\zeta),$$

where $\mathbf{x}_i$ is the location of the ith controlling point and ϕ_i is the base function as follows [28],

$$\begin{aligned}&\phi_1=(-1+\zeta+\eta+\xi)(-1+2\zeta+2\eta+2\xi),\\&\phi_2=\xi(-1+2\xi),\quad \phi_3=\eta(-1+2\eta),\quad \phi_4=\zeta(-1+2\zeta),\\&\phi_5=-4\xi(-1+\zeta+\eta+\xi),\quad \phi_6=4\eta\xi,\\&\phi_7=-4\eta(-1+\zeta+\eta+\xi),\quad \phi_8=-4\zeta(-1+\zeta+\eta+\xi),\\&\phi_9=4\zeta\xi,\quad \phi_{10}=4\zeta\eta.\end{aligned} \tag{36}$$

Then, the integration of monomial in Eq. (35) becomes

$$\int_\Omega x^{k_1}y^{k_2}z^{k_3}\mathrm{d}x\mathrm{d}y\mathrm{d}z=\int_{\hat{\Omega}}x^{k_1}y^{k_2}z^{k_3}(\xi,\eta,\zeta)\left|\frac{\partial(x,y,z)}{\partial(\xi,\eta,\zeta)}\right|\mathrm{d}\xi\mathrm{d}\eta\mathrm{d}\zeta. \tag{37}$$

It can be evaluated numerically as

$$\iiint_\Omega x^{k_1}y^{k_2}z^{k_3}\mathrm{d}x\mathrm{d}y\mathrm{d}z=\sum_{m=1}^{M}\omega_m x^{k_1}y^{k_2}z^{k_3}(\xi,\eta,\zeta)_m\left|\frac{\partial(x,y,z)}{\partial(\xi,\eta,\zeta)}\right|_m\Delta\xi\Delta\eta\Delta\zeta, \tag{38}$$

where ω_m is the quadrature weight at the Gaussian point $(\xi,\eta,\zeta)_m$ and $\Delta\xi=\Delta\eta=\Delta\zeta=1$. A five-point Gaussian quadrature with fourth-order spatial accuracy is used with

$$\begin{aligned}&(\xi,\eta,\zeta)_1=(\tfrac{1}{4},\tfrac{1}{4},\tfrac{1}{4}),\ (\xi,\eta,\zeta)_2=(\tfrac{1}{2},\tfrac{1}{6},\tfrac{1}{6}),\ (\xi,\eta,\zeta)_3=(\tfrac{1}{6},\tfrac{1}{6},\tfrac{1}{6}),\\&(\xi,\eta,\zeta)_4=(\tfrac{1}{6},\tfrac{1}{6},\tfrac{1}{2}),\ (\xi,\eta,\zeta)_5=(\tfrac{1}{6},\tfrac{1}{2},\tfrac{1}{6}),\end{aligned}$$

with $\omega_1=-\frac{2}{15}$, $\omega_m=\frac{3}{40}$, $m=2,3,4,5$.

4.1.1. Stencil for polynomial $P^2(\boldsymbol{x})$

In order to achieve a third-order spatial accuracy, the quadratic polynomial $P^2(\mathbf{x})$ on Ω_0 is constructed on the compact stencil S_2 including Ω_0 and its all von Neumann neighbors, $\Omega_m, m=1,\ldots,4$, where the averages of $Q(\mathbf{x})$ and averaged derivatives of $Q(\mathbf{x})$ over each cell are known.

The following values on S_2 are used to obtain $P^2(\mathbf{x})$,

- cell averages $\overline{Q}$ for cell 0, 1, 2, 3, 4;
- cell averages of the x-direction partial derivative $\overline{Q}_{x_1}$ for cell 1, 2, 3, 4;
- cell averages of the y-direction partial derivative $\overline{Q}_{x_2}$ for cell 1, 2, 3, 4;
- cell averages of the z-direction partial derivative $\overline{Q}_{x_3}$ for cell 1, 2, 3, 4.

The polynomial $P^2(\mathbf{x})$ is required to exactly satisfy

$$\iiint_{\Omega_m}P^2(\mathbf{x})\mathrm{d}V=\overline{Q}_m\left|\Omega_m\right|, \tag{39}$$

where $\overline{Q}_m$ is the cell averaged value over Ω_m, $m=1,\ldots,4$, with the following condition satisfied in a least-square sense

$$\begin{aligned}&\iiint_{\Omega_m}\frac{\partial}{\partial x_1}P^2(\mathbf{x})\mathrm{d}V=(\overline{Q}_{x_1})_m|\Omega_m|,\\&\iiint_{\Omega_m}\frac{\partial}{\partial x_2}P^2(\mathbf{x})\mathrm{d}V=(\overline{Q}_{x_2})_m|\Omega_m|,\\&\iiint_{\Omega_m}\frac{\partial}{\partial x_3}P^2(\mathbf{x})\mathrm{d}V=(\overline{Q}_{x_3})_m|\Omega_m|,\end{aligned} \tag{40}$$

where $\overline{Q}_{x_i}, i = 1, 2, 3$ are the cell averaged directional derivatives over Ω_m in a global coordinate, respectively. On a regular mesh, the system has 16 independent equations. The constrained least-square method is used to solve the above linear system [13]. The above reconstruction improves the linear stability of the scheme and increases the CFL number. The numerical experiments show that it also reduces the numerical errors compared with the unconstrained least-square technique. The left and right states $W^{l,r}$ provided by the reconstructed $P^2(\mathbf{x})$ yields a linearly stable third-order compact GKS, as validated through numerical tests in Section 5.

4.1.2. Stencils for polynomials $P^1(\mathbf{x})$ and $P^0(\mathbf{x})$

In order to deal with discontinuity, lower-order polynomials from the sub-stencils should be determined. Following the multi-resolution reconstruction in [39], the first-order polynomial $P^1(\mathbf{x})$ is determined from the same central stencil as the $P^2(\mathbf{x})$ but only with the cell-averaged conservative variables

- $\overline{Q}$ for cell 0, 1, 2, 3, 4.

The polynomial $P^1(\mathbf{x})$ is required to satisfy

$$\iiint_{\Omega_m} P^1(\mathbf{x})\mathrm{d}V = \overline{Q}_m \left|\Omega_m\right|, \quad m = 1, 2, 3, 4, \tag{41}$$

in a least-square sense.

Note that the left and right states $W^{l,r}$ solely determined by the reconstructed $P^1(\mathbf{x})$ yield an unstable second-order GKS. The theoretical proof for such an instability on the second-order Riemann solver-based-FVM can be found in [5]. The zeroth-order polynomial $P^0(\mathbf{x})$ is simply determined by the cell-averaged conservative variables on the targeted cell Ω_0 itself, i.e. $P^0(\mathbf{x}) = \overline{Q}_0$. The coefficient matrices for the above $P^j(\mathbf{x}), j = 0, 1$ are always invertible.

4.2. Multi-resolution WENO procedure

Define three polynomials

$$\begin{aligned} p_2(\mathbf{x}) &= \frac{1}{\gamma_{2,2}} P^2(\mathbf{x}) - \sum_{\ell=0}^{1} \frac{\gamma_{\ell,2}}{\gamma_{2,2}} p_\ell(\mathbf{x}), \\ p_1(\mathbf{x}) &= \frac{1}{\gamma_{1,1}} P^1(\mathbf{x}) - \frac{\gamma_{0,1}}{\gamma_{1,1}} P^0(\mathbf{x}), \\ p_0(\mathbf{x}) &= P^0(\mathbf{x}). \end{aligned} \tag{42}$$

For a third-order reconstruction, the second-order polynomial $P^2(\mathbf{x})$ can be rewritten as

$$P^2(\mathbf{x}) = \gamma_{2,2} p_2 + \gamma_{1,2} p_1 + \gamma_{0,2} p_0 \tag{43}$$

with arbitrary positive coefficients $\gamma_{m,n}$ satisfying $\gamma_{0,2} + \gamma_{1,2} + \gamma_{2,2} = 1, \gamma_{0,1} + \gamma_{1,1} = 1$.

For a second-order reconstruction, the first-order polynomial $P^1(\mathbf{x})$ can be rewritten as

$$P^1(\mathbf{x}) = \gamma_{1,1} p_1 + \gamma_{0,1} p_0 \tag{44}$$

with arbitrary positive coefficients $\gamma_{m,n}$ satisfying $\gamma_{0,1} + \gamma_{1,1} = 1$. The coefficients are chosen as $\gamma_{2,2} : \gamma_{1,2} : \gamma_{0,2} = 100 : 10 : 1$, and $\gamma_{1,1} : \gamma_{0,1} = 10 : 1$ as suggested in [39].

The smoothness indicators $\beta_j, j = 1, 2$ are defined as

$$\beta_j = \sum_{|\alpha|=1}^{r_j} |\Omega|^{\frac{2}{3}|\alpha|-1} \iiint_{\Omega} \left(D^\alpha P_j(\mathbf{x})\right)^2 \mathrm{d}V, \tag{45}$$

where α is a multi-index and D is the derivative operator, $r_1 = 1$, $r_2 = 2$. The smoothness indicators in Taylor series at (x_0, y_0) have the order

$$\begin{aligned} \beta_2 &= O\{|\Omega_0|^{\frac{2}{3}}[1 + O(|\Omega_0|^{\frac{2}{3}})]\} = O(|\Omega_0|)^{\frac{2}{3}} = O(h^2), \\ \beta_1 &= O\{|\Omega_0|^{\frac{2}{3}}[1 + O(|\Omega_0|^{\frac{1}{3}})]\} = O(|\Omega_0|)^{\frac{2}{3}} = O(h^2). \end{aligned}$$

Assuming a suitable β_0,

$$\beta_0 = O\{|\Omega_0|^{\frac{2}{3}}[1 + O(|\Omega_0|^{\frac{1}{3}})]\} = O(|\Omega_0|)^{\frac{2}{3}} = O(h^2),$$

a global smoothness indicator σ similar to that in [39] can be defined

$$\sigma^{3rd} = \left(\frac{1}{2}(|\beta_2 - \beta_1| + |\beta_2 - \beta_0|)\right)^{\frac{4}{3}} = O(|\Omega_0|^2) = O(h^4),$$

and

$$\sigma^{2nd} = |\beta_1 - \beta_0|^{\frac{4}{3}} = O(|\Omega_0|^2) = O(h^4).$$

Then, the corresponding non-linear weights are given by

$$\begin{aligned} \omega_{m,n} &= \gamma_{m,n}(1 + (\frac{\sigma}{\epsilon + \beta_m})^2), \\ \bar{\omega}_{m,n} &= \frac{\bar{\omega}_{m,n}}{\sum \omega_{m,n}} = \gamma_{m,n} + O(h^4), \end{aligned} \tag{46}$$

where $m = 0, 1, 2$ for $n = 2$ and $m = 0, 1$ for $n = 1$, and ϵ takes 10^{-8} to avoid zero in the denominator.

Replacing $\gamma_{m,n}$ by the normalized non-linear weights $\bar{\omega}_{m,n}$ in Eq. (43) and Eq. (44), the final reconstructed polynomials are given by

$$R^{3rd}(\mathbf{x}) = \bar{\omega}_{2,2}p_2 + \bar{\omega}_{1,2}p_1 + \bar{\omega}_{0,2}p_0 \tag{47}$$

for a third-order spatial accuracy, and

$$R^{2nd}(\mathbf{x}) = \bar{\omega}_{1,1}p_1 + \bar{\omega}_{0,1}p_0 \tag{48}$$

for a second-order spatial accuracy.

As a result, the non-linear reconstruction meets the requirement for a third-order accuracy $R(\mathbf{x}) = P(\mathbf{x}) + O(h^3)$. If any of these values yield negative density or pressure, the first-order reconstruction is used instead. The desired non-equilibrium states at Gaussian points can be obtained from the weighted polynomials

$$Q^{l,r}_{p,k} = R^{l,r}(\mathbf{x}_{p,k}),\ (Q^{l,r}_{x_i})_{p,k} = \frac{\partial R^{l,r}}{\partial x_i}(\mathbf{x}_{p,k}). \tag{49}$$

4.3. A two-step reconstruction

According to the definition in Eq. (45), the smooth indicator of the zeroth-order polynomial $P^0(\mathbf{x})$ is always 0. So, a new smooth indicator for $P^0(\mathbf{x})$ has to be defined and can be given as a non-linear combination of the first-order biased sub-stencils as suggested in [39]. One of the choices is

$$\begin{aligned} &P^1_1 \text{ on } S_1 = \{\bar{Q}_0, \bar{Q}_1, \bar{Q}_2, \bar{Q}_3\}, \quad P^1_2 \text{ on } S_2 = \{\bar{Q}_0, \bar{Q}_1, \bar{Q}_2, \bar{Q}_4\}, \\ &P^1_3 \text{ on } S_3 = \{\bar{Q}_0, \bar{Q}_1, \bar{Q}_3, \bar{Q}_4\}, \quad P^1_4 \text{ on } S_4 = \{\bar{Q}_0, \bar{Q}_2, \bar{Q}_3, \bar{Q}_4\}. \end{aligned}$$

In this plan, a total of $16 \times 9 + 3 \times 4 + 3 \times 3 \times 5 = 192$ words is required on each cell for reconstruction. Different from that proposed in [39], the plan above is compact. The plan in [39] is non-compact, e.g., one of the sub-stencils is $\hat{P}^1_1$ on $\hat{S}_1 = \{\bar{Q}_0, \bar{Q}_1, \bar{Q}_2, \bar{Q}_3, \bar{Q}_4\}$. Note that $\bar{Q}_4$ is the neighbor-neighbor cell. Therefore, our plan has a better mesh adaptability. However, since only compact information is used, this plan shows poor robustness for the third-order reconstruction since the coefficient matrices for these sub-stencils can be close to singular under poor mesh quality. In other words, the smooth indicators for P^0 can be greater than those of P^1 and P^2 under irregular mesh and the WENO will fail to suppress oscillations.

Inspired by the method in [31], a two-step reconstruction is designed as follows to maintain the compact manner of the scheme:

- Reconstruction Step 1: Construct the first-order polynomial $P^1(\mathbf{x})$ in each cell by Eq. (41). Compute the slopes, e.g., b_1, b_2, b_3 for each component, and store them. A coefficient matrix with dimension 3×4 is stored for $P^1(\mathbf{x})$ and another matrix with dimension 5×3 for the slopes.
- Reconstruction Step 2: Conduct the multi-resolution reconstruction for each cell, and the smooth indicator β_0 for $P^0(\mathbf{x})$ is given as a non-linear combination of the smooth indicators of $P^1_j(\mathbf{x})$ from the neighbor cells, i.e.,

$$\begin{aligned} \beta_{0,j} &= |\Delta_0|(b^2_{1,j} + b^2_{2,j} + b^2_{3,j}), \\ \sigma^{1st} &= (\frac{1}{6}(\sum |\beta_{0,j} - \beta_{0,k}|))^{\frac{4}{3}}, \\ \omega^{1st}_j &= 1 + \frac{\sigma^{1st}}{\epsilon + \beta_j}, \\ \bar{\omega}^{1st}_j &= \frac{\omega_j}{\sum \omega_j}, \\ \beta_0 &= \sum \bar{\omega}^{1st}_j \beta_{0,j}, \end{aligned} \tag{50}$$

  where $j, k = 1, 2, 3, 4$ and $j > k$. Then, the second-order reconstruction is complete.

For the third-order reconstruction, only one extra beta β_2 in Eq. (45) is needed. A coefficient matrix with dimension 9×16 is stored for $P^2(\mathbf{x})$.

Through the reconstruction step 1, the sub-stencils are extended to neighboring cells of the neighbors. Compared with the first plan, the robustness and mesh adaptability is significantly improved. $16 \times 9 + 3 \times 4 + 3 \times 5 = 171$ words are required on each cell for the two-step reconstruction, which is even less than the first plan. However, one more communication is needed if the code is parallelized on different nodes. In this paper, only the numerical results based on the two-step reconstruction are presented.

4.4. Reconstruction for the boundary cells

The strategy of the two-step and multi-resolution reconstruction are extended to the boundary condition treatment. The one-sided reconstruction without ghost cell is adopted here with special care on Dirichlet boundary condition, i.e. the non-slip adiabatic wall and the non-slip isothermal one. For the non-slip adiabatic boundary, the velocities are constrained. For the non-slip isothermal boundary condition, both the velocities and the temperature are constrained.

- Reconstruction Step 1.
  For ith (i = 0,...,4) conservative variables:
  - If there is no constraint for all the boundary faces:
    - If the neighboring cell number is no less than 3, construct the first-order polynomial $P^1(\mathbf{x})$. If the coefficient matrix is found to be nearly singular, which suggesting a poor mesh quality, set $P^1(\mathbf{x}) = P^0(\mathbf{x})$.
    - If the neighboring cell number is less than 3, use the cell-averaged slopes as the slopes of the first-order polynomial instead.
  - If there exists at least one constraint for all the boundary faces on the targeted cell, the weighted constrained least square reconstruction involving all the neighboring cells and boundary faces are conducted. The weights for those boundary faces that do not have constraint are set to be zero. In this step, each constrained boundary face has one constraint, which is located at the geometric center of the face.
    - If the sum of the neighboring cell number and the constraint number is no less than 3, and the constraint number is no greater than 3, construct the first-order polynomial $P^1(\mathbf{x})$ by using constrained least-square method.
    - If the constraint number is greater than 3 (which is impossible for tetrahedron mesh), construct the first-order polynomial $P^1(\mathbf{x})$ by using the least-square method.
    - If the sum of the neighboring cell number and the constraint number is less than 3, use the cell-averaged slopes as the slopes of the first-order polynomial instead.

    For non-slip adiabatic wall, each component is reconstructed in the following order.
    - Step 1. One-sided reconstruction for density.
    - Step 2. One-sided constrained reconstruction for momentum $\rho\mathbf{U} = \rho\mathbf{U}_{wall}$ where the reconstructed density is used.
    - Step 3. One-sided reconstruction for energy.

    For non-slip isothermal wall, each component is reconstructed in the following order.
    - Step 1. One-sided reconstruction for density.
    - Step 2. One-sided constrained reconstruction for momentum $\rho\mathbf{U} = \rho\mathbf{U}_{wall}$ where the reconstructed density is used.
    - Step 3. One-sided constrained reconstruction for energy $\rho E = \frac{1}{2}\rho\mathbf{U}_{wall}^2 + \rho T_{wall}/(r-1)$, where the reconstructed density is used.
- Reconstruction Step 2.
  For a second-order reconstruction, the WENO procedure in Eq. (48) is complete. If a third-order reconstruction is adopted, the second-order polynomial $P^2(\mathbf{x})$ is needed. For the ith (i = 0,...,4) conservative variables:
  - If there is no constraint for all the boundary faces:
    - If the neighboring cell number is no less than 3 and the coefficient matrix is not singular, construct the second-order polynomial $P^2(\mathbf{x})$, by constraining the cell-averaged values. Otherwise, the first-order polynomial from the $P^2(\mathbf{x})$ stencils will be constructed in a least-squares sense.
    - For the smooth reconstruction, the first-order polynomial using the $P^2(\mathbf{x})$ stencils is reconstructed instead.
  - If there exists at least one constrained face on the targeted cell, the weighted constrained least square reconstruction involving all the neighbor cells and boundary faces are conducted. The weights for those boundary faces that do not have constraint are set to be zero. Each constrained triangular face has three constraints, which are located at the corresponding Gaussian points.
    - If the sum of the numbers of neighboring cell-averaged data and the constraint are no less than 9, and the constraint number is no greater than 9, construct the first-order polynomial $P^1(\mathbf{x})$ by using constrained least-square method.
    - If the constraint number is greater than 9 (which never happens in the tests of this paper), construct the first-order polynomial using the $P^2(\mathbf{x})$ stencils by the weighted least-square instead.
    - If the sum of neighboring cell-averaged data and the constraint number is less than 9, construct the first-order polynomial using the $P^2(\mathbf{x})$ stencil by the weighted least-square instead.

    The constrained quantities and reconstruction order for the non-slip wall boundaries are the same as those in the reconstruction step 1.

It should be emphasized that the above criteria are general for other types of mesh and hybrid mesh. After obtaining the inner state (assume as $\tilde{\mathbf{W}}^r$) at a boundary Gaussian point, a ghost state (assume as $\tilde{\mathbf{W}}^l$) can be assigned according to boundary condition under local coordinates. There is possible discontinuity between $\tilde{\mathbf{W}}^l$ and $\tilde{\mathbf{W}}^r$ if the WENO reconstruction is used. The ghost state setting at the solid wall boundary is given as follows (the tilde is omitted).

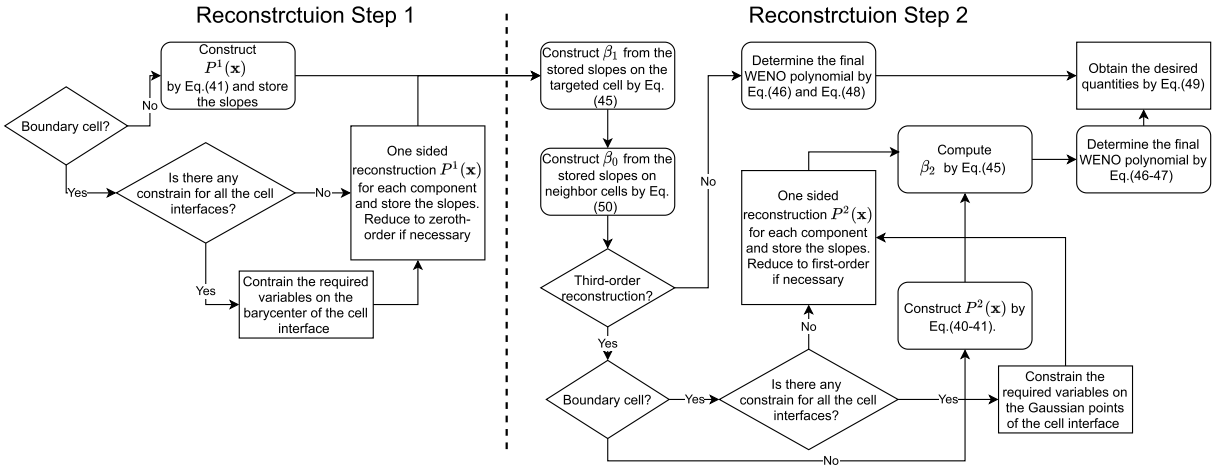

Fig. 2. The process of the compact two-step multi-resolution reconstruction.

- Slip wall. The conservative variables under local coordinate $(\rho, \rho U_1, \rho U_2, \rho U_3, \rho E)^l = (\rho, -\rho U_1, \rho U_2, \rho U_3, \rho E)^r$. The normal derivatives $(\rho U_1)^l_{x_1} = (\rho U_1)^r_{x_1}$ while the normal derivatives for other components are $W^l_{i_{x_1}} = -W^r_{i_{x_1}}, \quad i = 0, 2, 3, 4$. The tangential derivatives $(\rho U_1)^l_{x_j} = -(\rho U_1)^r_{x_j}, \quad j = 2, 3$ while the tangential derivatives for other components are $W^l_{i_{x_j}} = W^r_{i_{x_j}}, \quad i = 0, 2, 3, 4, \quad j = 2, 3$.
- Non-slip adiabatic wall. The conservative variables under local coordinate are given as $(\rho, \rho U_1, \rho U_2, \rho U_3, \rho E)^l = (\rho, -\rho U_1, -\rho U_2, -\rho U_3, \rho E)^r$. The derivatives for all momenta $(\rho U_i)^l_{x_j} = (\rho U_i)^r_{x_j}, \quad i = 1, 2, 3, \quad j = 1, 2, 3$, while the normal derivatives for other components are $W^l_{i_{x_j}} = -W^r_{i_{x_j}}, \quad i = 0, 4, \quad j = 1, 2, 3$.
- Non-slip isothermal wall.
  - Assume the same pressure $p^l = p^r$. The velocity is opposite $U^l_i = -U^r_i, \quad i = 1, 2, 3$. The temperature is set as $T^l = 2T^0 - T^r$, where $T_0 = T_{wall}$. Then, $\rho^l = p^l / RT^l = p^r / RT^l = p^r / R(2T^0 - T^r)$.
  - Use primitive variables $(\rho, \mathbf{U}, p)^l$ to get $(\rho, \mathbf{U}, \rho E)^l$.
  - From the chain rule, $\partial U_i = \frac{\partial(\rho U_i) - \partial \rho U_i}{\rho} \quad i = 1, 2, 3$. Denote $Q = \frac{1}{2}\sum U_i^2$, $\partial Q = \sum \partial U_i U_i$. Then, $\partial \rho E = \partial \rho Q + \partial Q \rho + \frac{1}{\gamma - 1}\partial p$ and $\partial p = (\gamma - 1)(\partial \rho E - \partial \rho Q - \partial Q \rho)$. From $p = \rho RT$, $\partial T = \frac{\partial p - R \partial \rho T}{R\rho}$ is obtained. And $\partial U^l_i, i = 1, 2, 3$, ∂p^l, and ∂T^l are determined.
  - The derivatives of the primitive variables for the ghost states are set as $\partial U^l_i = \partial U^r_i, \quad i = 1, 2, 3$. $\partial T^l = \partial T^r$. $\partial p^l = -\partial p^r$.
  - Then, obtain $\partial \rho^l$ by $\partial \rho = \frac{\partial p - R \partial T \rho}{RT}$ and $\partial(\rho U_i)^l$ by $\partial(\rho U_i) = \partial \rho U_i + \partial U_i \rho$.
  - Finally, get $\partial(\rho E)^l$ by $\partial \rho E = \partial \rho Q + \partial Q \rho + \frac{1}{\gamma - 1}\partial p$.

A summary for the reconstruction procedure is shown in Fig. 2.

4.5. Reconstruction of the equilibrium state

The reconstructions for the non-equilibrium states have the same spatial order and can be used to get the equilibrium state $g^c, g^c_{x_i}$ directly by a suitable average of $g^{l,r}, g^{l,r}_{x_i}$. To be consistent with the construction of g^c, we make an analogy of the kinetic-based weighting method for $g^c_{x_i}$, which are given by

$$\begin{aligned}
&\int \boldsymbol{\psi} g^c \mathrm{d}\Xi = \mathbf{W}^c = \int_{u>0} \boldsymbol{\psi} g^l \mathrm{d}\Xi + \int_{u<0} \boldsymbol{\psi} g^r \mathrm{d}\Xi, \\
&\int \boldsymbol{\psi} g^c_{x_i} \mathrm{d}\Xi = \mathbf{W}^c_{x_i} = \int_{u>0} \boldsymbol{\psi} g^l_{x_i} \mathrm{d}\Xi + \int_{u<0} \boldsymbol{\psi} g^r_{x_i} \mathrm{d}\Xi.
\end{aligned} \tag{51}$$

The data for this method has compact support. In programming, this procedure is included inside the subroutine of the gas distribution function, since it is performed at the local coordinate. Thus, it is also cache-friendly. This method has been validated in the non-compact WENO5-GKS [8]. In this way, all components of the microscopic slopes in Eq. (26) have been fully obtained. It is worth to remark that the above reconstruction procedure can be directly implemented to arbitrary mesh.

5. Numerical examples

In this section, numerical tests will be presented to validate the proposed scheme. The time step is determined by

$$\Delta t = C_{CFL} \mathrm{Min}\left(\frac{\Delta r_i}{|\mathbf{U}_i| + (a_s)_i}, \frac{(\Delta r_i)^2}{3\nu_i}\right), \tag{52}$$

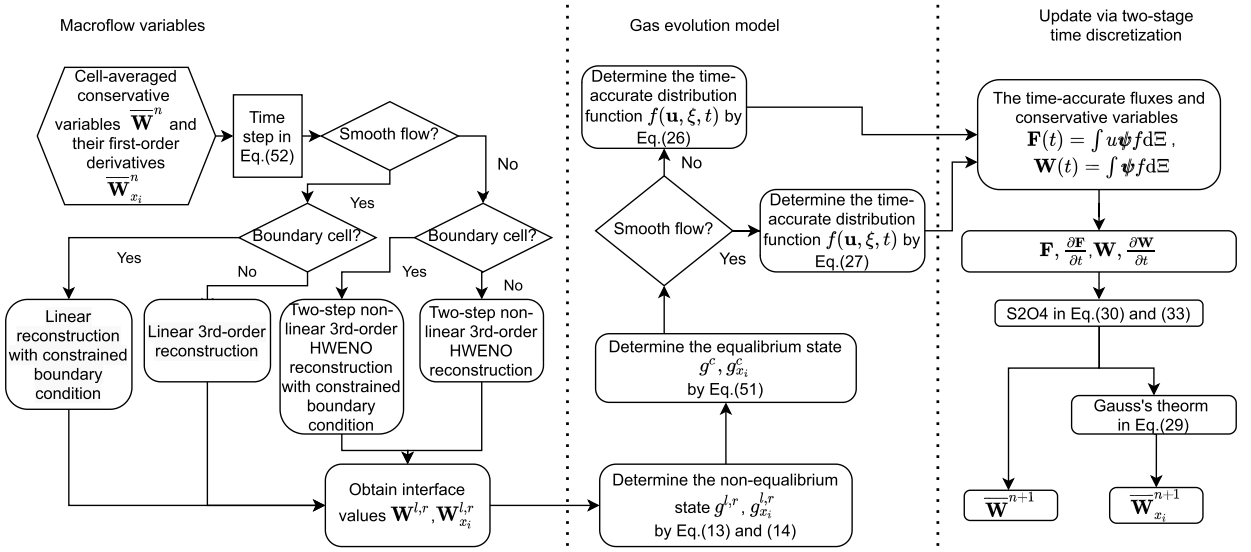

Fig. 3. The brief algorithm of the compact GKS.

where C_{CFL} is the CFL number, and $|\mathbf{U}_i|$, $(a_s)_i$, and $\nu_i = (\mu/\rho)_i$ are the magnitude of velocities, sound speed, and kinematic viscosity coefficient for cell i. The Δr_i is taken as the approximated inscribed sphere radius of a tetrahedron,

$$\Delta r_i = \frac{3|\Omega_i|}{\sum |\Gamma_{ip}|}.$$

All reconstructions will be performed on the conservative variables. Quadratic elements and a $CFL = 1$ are used if no specified. An algorithm flowchart of the compact GKS is given in Fig. 3.

5.1. 3-D sinusoidal wave propagation

The advection of density perturbation is tested with the initial condition

$$\rho(x,y,z) = 1 + 0.2\sin(\pi(x+y+z)),$$
$$\mathbf{U}(x,y,z) = (1,1,1), \quad p(x,y,z) = 1,$$

within a cubic domain $[0,2]\times[0,2]\times[0,2]$. In the computation, a series of uniform meshes with $6\times N^3$ cells are used. With the periodic boundary condition in all directions, the analytic solution is

$$\rho(x,y,z,t) = 1 + 0.2\sin(\pi(x+y+z-t)),$$
$$\mathbf{U}(x,y,z) = (1,1,1), \quad p(x,y,z,t) = 1.$$

The collision time $\tau = 0$ is set since the flow is smooth and inviscid. The L^1, L^2 and L^∞ errors and the corresponding orders with linear and non-linear Z-type weights at $t = 2$ for the third-order compact GKS are given in Table 1 and Table 2. On the same mesh, the errors of the current CGKS are smaller than those provided in the third-order non-compact FVM [39]. For example, on the 6×20^3 mesh, the L^1 error is 3.29e-4 for CGKS while 1.79e-3 for FVM [39]. The stability proof for the present spatial-temporal coupled scheme under the tetrahedral mesh needs future study. The result with non-linear Z-type weights for the second-order scheme is also presented in Table 3. Expected accuracy is achieved for all cases. Note that the errors from the WENO nonlinear weights are usually larger than those from the linear scheme on a coarse mesh, and they will become the same on a fine mesh. This is a general observation of WENO-type schemes. It is worth remarking that the improved nonlinear reconstruction, such as TENO, might overcome this problem [11] and future study is needed.

5.2. One dimensional Riemann problems

(a) Shu-Osher problem

This is the Shu-Osher problem [26] with the initial condition

$$(\rho, U, p) = \begin{cases} (3.857143, 2.629369, 10.33333), & 0 < x \le 1, \\ (1 + 0.2\sin(5x), 0, 1), & 1 < x < 10. \end{cases}$$

Table 1
Accuracy test for the 3D sin-wave propagation by the linear third-order compact reconstruction. CFL = 1.0.

Mesh number	L^1 error	Order	L^2 error	Order	L^∞ error	Order
6×5^3	2.220404e-02		2.458004e-02		3.674171e-02	
6×10^3	2.714856e-03	3.03	3.035792e-03	3.02	4.794437e-03	2.94
6×20^3	3.285843e-04	3.05	3.666555e-04	3.05	6.093576e-04	2.98
6×40^3	4.360713e-05	2.92	4.862997e-05	2.91	8.411243e-05	2.87

Table 2
Accuracy test for the 3D sin-wave propagation by the third-order compact HWENO reconstruction with $d_0 : d_1 : d_2 = 100 : 10 : 1$. CFL = 1.0.

Mesh number	L^1 error	Order	L^2 error	Order	L^∞ error	Order
6×5^3	4.119490e-02		4.675556e-02		7.211452e-02	
6×10^3	6.593180e-03	2.64	8.682551e-03	2.43	2.501214e-02	1.53
6×20^3	4.217035e-04	3.97	5.481270e-04	3.99	1.251195e-03	4.32
6×40^3	4.287225e-05	3.30	4.947759e-05	3.47	1.138919e-04	3.46

Table 3
Accuracy test for the 3D sin-wave propagation by the second-order WENO reconstruction with $d_0 : d_1 = 10 : 1$. CFL = 1.0.

mesh number	L^1 error	Order	L^2 error	Order	L^∞ error	Order
6×5^3	2.705626e-02		3.377431e-02		6.219542e-02	
6×10^3	6.963215e-03	1.96	7.839272e-03	2.10	1.311175e-02	1.37
6×20^3	2.370280e-03	1.55	2.640328e-03	1.57	4.165732e-03	1.65
6×40^3	6.351481e-04	1.90	7.069711e-04	1.90	1.100743e-03	1.92

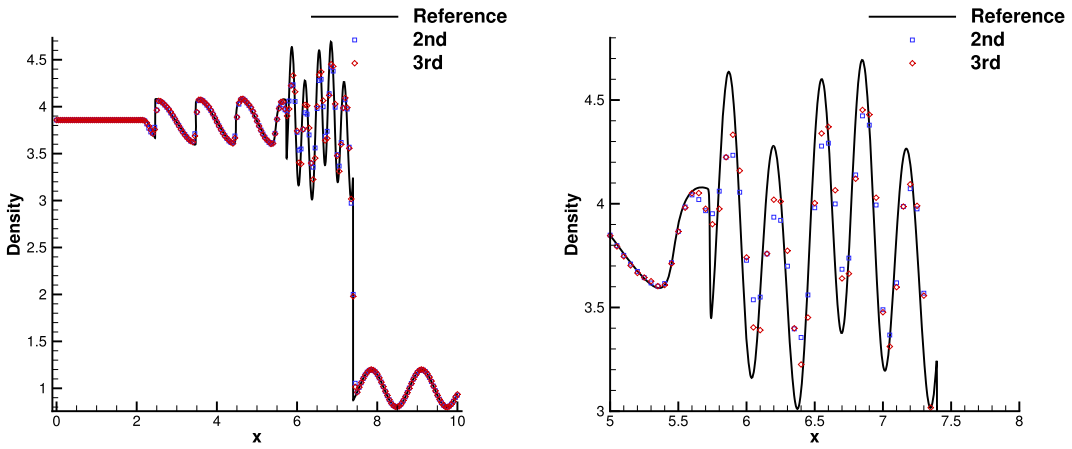

Fig. 4. Shu-Osher problem. Mesh number: $6\times200\times2\times2$. (For interpretation of the colors in the figure(s), the reader is referred to the web version of this article.)

The computational domain is $[0, 10]$. The non-reflecting boundary condition is given on the left boundary, and the fixed wave profile is extended on the right boundary. The computed density profiles and local enlargements at $t = 1.8$ with mesh size $1/200$ and $1/400$ are plotted in Fig. 4 and Fiq. 5. The third-order compact GKS shows a better resolution in resolving the sinusoidal wave than the second order method on the coarse mesh. Both schemes resolve the waves nicely with the fine mesh.

(b) Blast wave problem

The initial conditions for the blast wave problem [30] are given as follows

$$(\rho, u, p) = \begin{cases} (1, 0, 1000), 0 \le x < 0.1, \\ (1, 0, 0.01), 0.1 \le x < 0.9, \\ (1, 0, 100), 0.9 \le x \le 1. \end{cases}$$

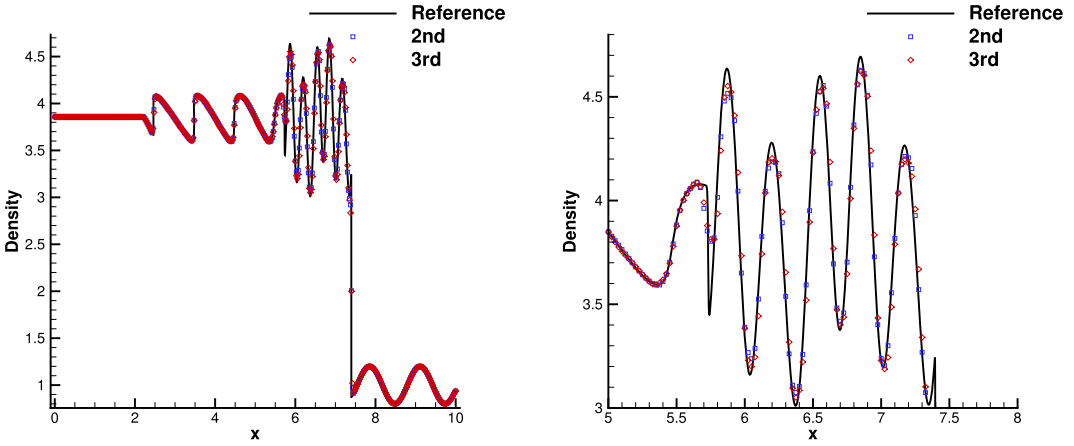

Fig. 5. Shu-Osher problem. Mesh number: $6 \times 400 \times 2 \times 2$.

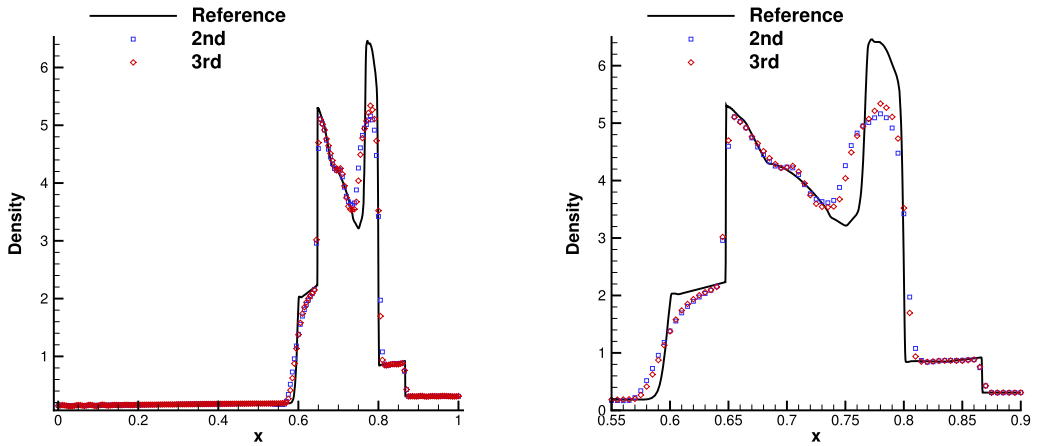

Fig. 6. Blastwave problem. Mesh number: $6 \times 200 \times 2 \times 2$.

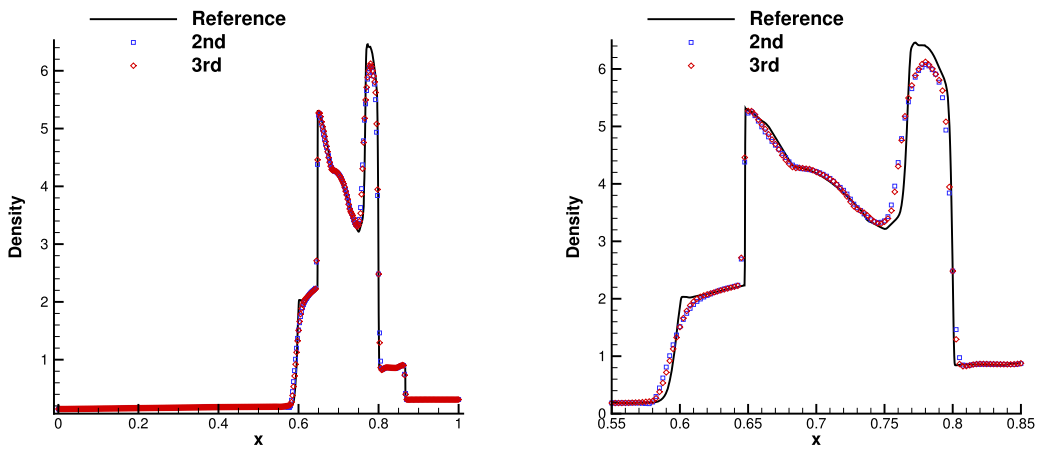

Fig. 7. Blastwave problem. Mesh number: $6 \times 400 \times 2 \times 2$.

In the computational domain, $6 \times 200 \times 2 \times 2$ and $6 \times 400 \times 2 \times 2$ mesh points are used. Reflection boundary conditions are applied at both ends. The density distributions at $t = 0.038$ are presented in Fig. 6 and Fig. 7. Both the second-order and third-order schemes show good robustness for such a strong shock-shock interaction.

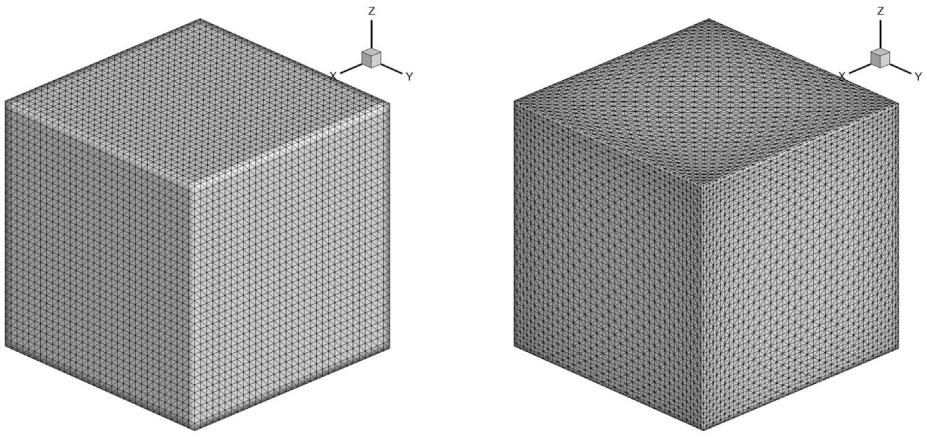

Fig. 8. Lid-driven cavity flow. Left: uniform mesh with near wall size $h = 1/32$. Right: non-uniform mesh with near wall size $h = 1/64$.

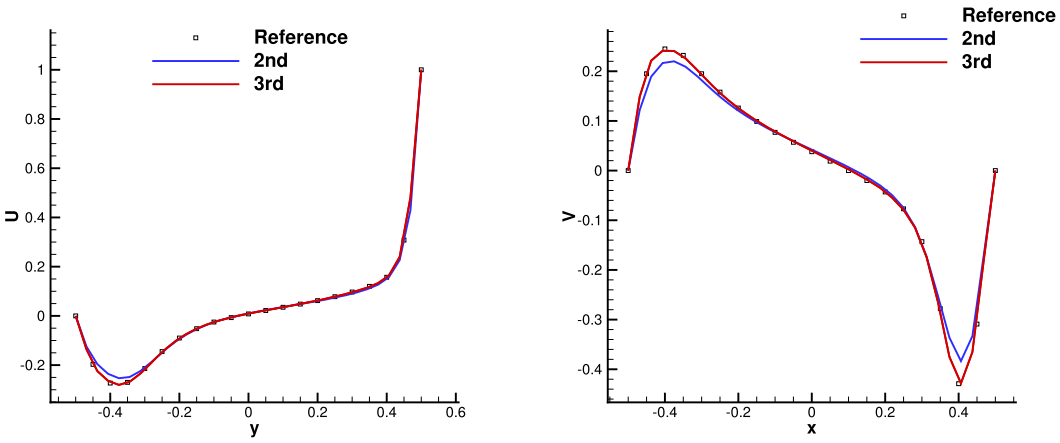

Fig. 9. Lid-driven cavity flow: Re = 1,000. The velocities profiles compared with the reference data in [24].

5.3. 3-D lid-driven cavity flow

A 3-D cavity is bounded in a unit cube and is driven by a uniform translation of the top boundary. In this case, the flow is simulated with Mach number $Ma = 0.15$ and $\gamma = 5/3$. All boundaries are isothermal and nonslip. The computational domain $[-0.5, 0.5] \times [-0.5, 0.5] \times [-0.5, 0.5]$ is covered by a uniform mesh with $6 \times 32 \times 32 \times 32$ points and a refined uniform mesh with $5 \times 40 \times 40 \times 40$ points, as shown in Fig. 8. A CFL number of 0.5 is used. The flow is initialized with $\rho = 1$, $U_1 = 0.15$, $U_2 = U_3 = 0$, and $p = 1/\gamma$. Since the flow is nearly incompressible and mesh is regular, the smooth reconstruction and the simplified solver in Eq. (26) are adopted in the computations. The simplified evolution solution in Eq. (27) from a continuous initial reconstruction at a cell interface has less numerical dissipation than the general GKS formula in Eq. (26) for the discontinuous flow. However, for low Mach numbers, with the increasing order of the reconstruction the general evolution model for discontinuous flow can also give very accurate results, as reported in [37].

(a) Re = 1,000

For the Reynolds number $Re = 1,000$, both results from the second-order and third-order reconstruction are presented under the uniform mesh. A low-order boundary treatment is used for the second-order scheme, which ensures a stable solution. The U-velocities along the line $x = 0, z = 0$, and V-velocities along the line $y = 0, z = 0$, are shown in Fig. 9. The velocity profiles from the third-order scheme match very well with the benchmark data [24]. The velocity magnitude contours and streamlines by the third-order scheme are shown in Fig. 10. The cavity case demonstrates the high-order accuracy of the compact GKS.

(b) Re = 3,200

The flow becomes transient when $Re > 2000$. Experimental results can be found in [20,21] at Re = 3200. The mean velocity and root-mean-square (RMS) velocity profiles are collected during a time interval, which corresponds to 7 to 10 minutes in the experiment [20] and 172 non-dimensional time in the simulation. The results obtained from the third-order scheme for the U velocity component along the line $x = 0, z = 0$, and the V velocity component along the line $y = 0, z = 0$ are presented in Fig. 11. Both results under the uniform mesh and the refined non-uniform mesh agree well with the experimental data. A better agreement in the RMS U-velocity U_{rms} can be observed in the refined mesh calculation.

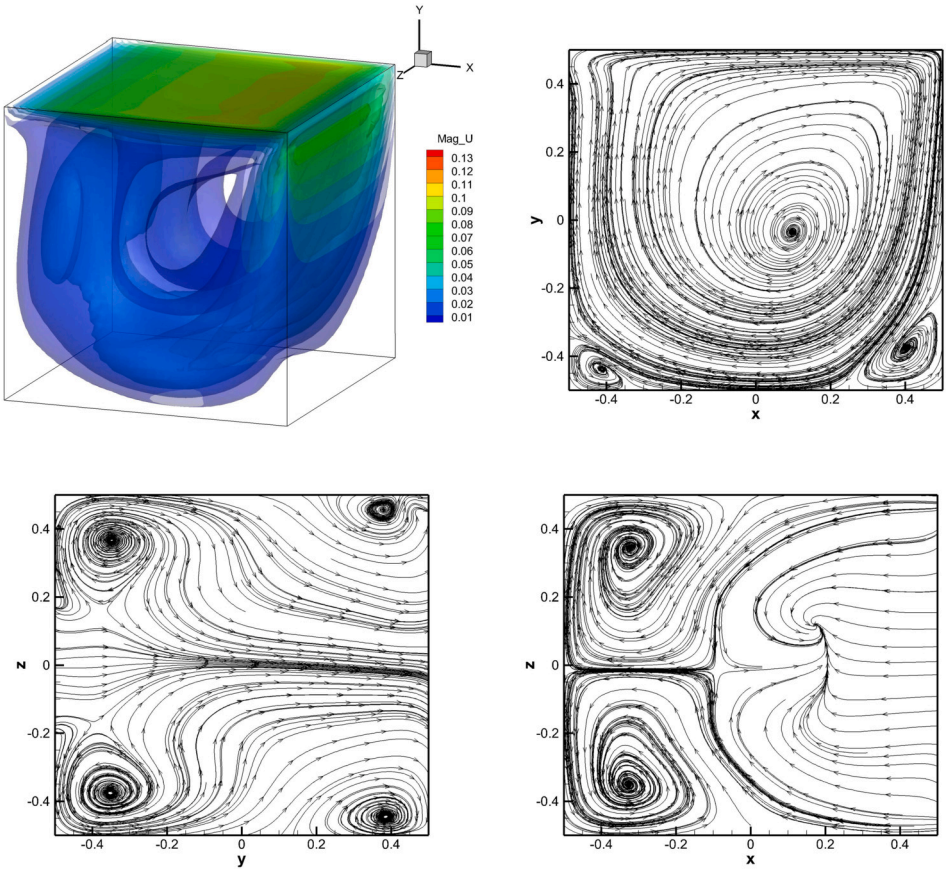

Fig. 10. Lid-driven cavity flow: Re = 1,000. Top left: The velocity magnitude contours. Others: The streamlines on $x = 0$, $y = 0$, and $z = 0$ planes.

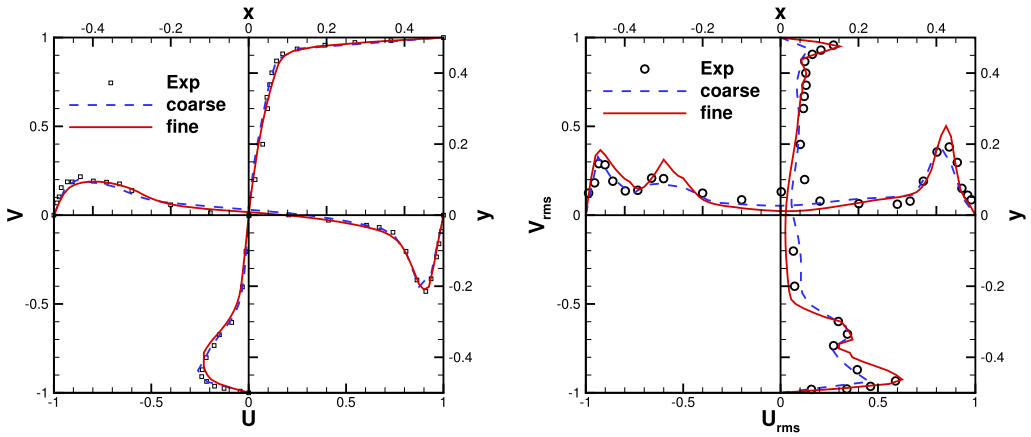

Fig. 11. Lid-driven cavity flow: Re = 3,200. The mean and RMS velocity profiles obtained by the third-order compact GKS are compared with the experimental data in [20,21].

5.4. Subsonic viscous flow around a sphere at Re = 118

A low-speed viscous flow passing through a sphere is tested. The Reynolds number based on the diameter of the sphere $D = 1$ is 118. In such case, a drag coefficient $C_D = 1$ was reported from the experiment in [27]. The far-field flow condition outside boundary of the domain is set with the free stream condition

$$(\rho, U, V, W, p)_\infty = (1, 0.2535, 0, 0, \frac{1}{\gamma}),$$

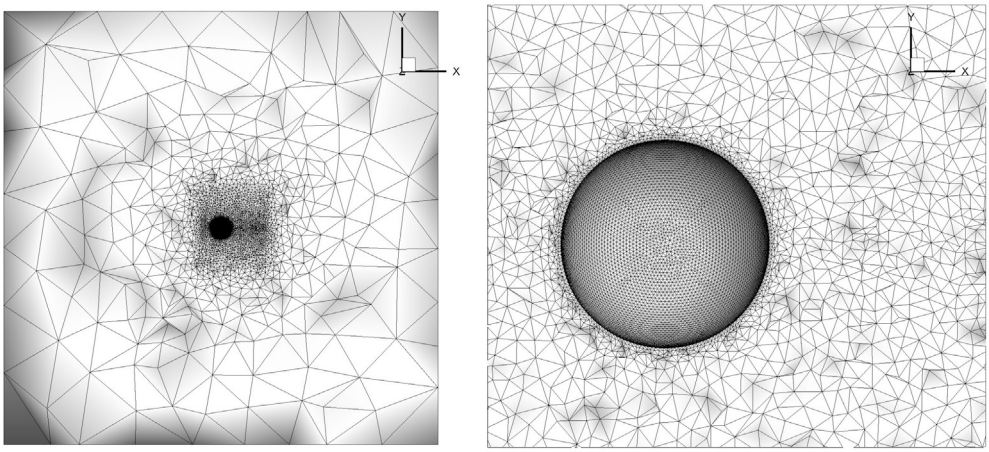

Fig. 12. Subsonic flow passing through a viscous sphere. Mesh number: 399,546.

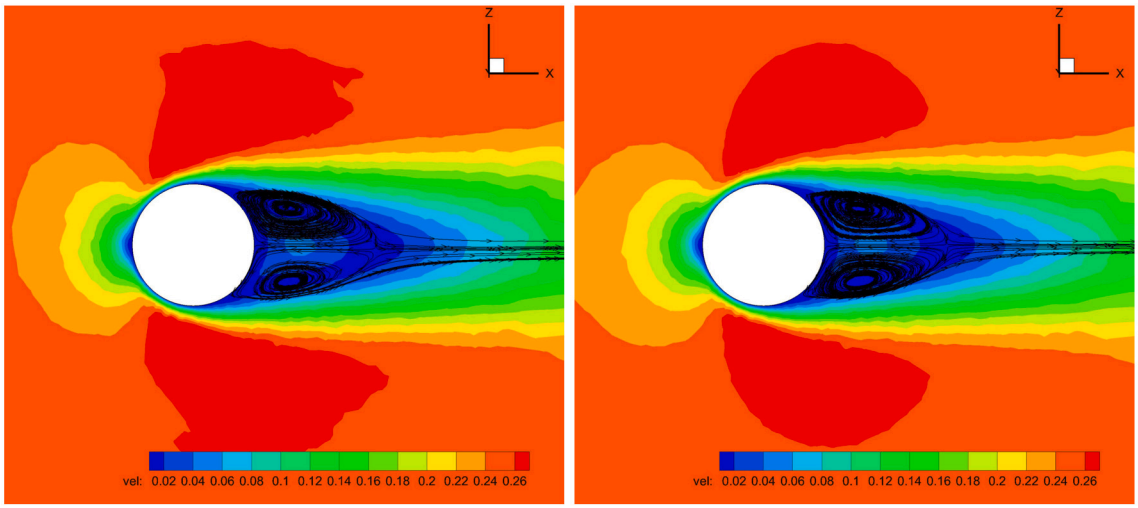

Fig. 13. Subsonic flow passing through a viscous sphere. Ma = 0.2535. Re = 118. Left: The second-order GKS. Right: The third-order GKS.

Table 4
Quantitative comparisons among different compact schemes for the viscous flow over a sphere.

Scheme	Mesh number	Cd	θ	L	Cl
Experiment [27]	–	1.0	122	1.07	–
Current 2nd	399,546	1.027	126.9	1.00	1.5e-2
Current 3rd	399,546	1.018	127.4	1.00	1.7e-3
Implicit third-order DDG [3]	160,868	1.016	123.7	0.96	–
Implicit fourth-order VFV [28]	458,915	1.014	–	–	2.0e-5
Implicit third-order AMR-VFV [18]	621,440	1.016	–	–	–

with $\gamma = 1.4$, $Ma_\infty = 0.2535$. The surface of the sphere is set as a non-slip adiabatic wall. The first mesh off the wall has a size $h \approx 1.5 \times 10^{-2} D$, as shown in Fig. 12. Both second-order and third-order schemes with non-linear reconstructions are tested. A clean and symmetric velocity contour is observed from the third-order compact GKS, as shown in Fig. 13. The pressure contour and the 3-D streamline are also presented in Fig. 14, where the high resolution from the non-linear compact reconstruction has been demonstrated, even with mesh irregularity. The quantitative results are given in Table 4, including the drag coefficient C_D, the separation angle θ, and the closest wake length L, as defined in [10].

5.5. Supersonic viscous flow passing through a sphere at Re = 300

To validate the robustness of the current scheme for the high-speed viscous flow, a supersonic flow passing through a sphere with $Ma = 1.2$ is tested. The non-slip adiabatic boundary condition is imposed on the surface of the sphere. The Reynolds number is 300

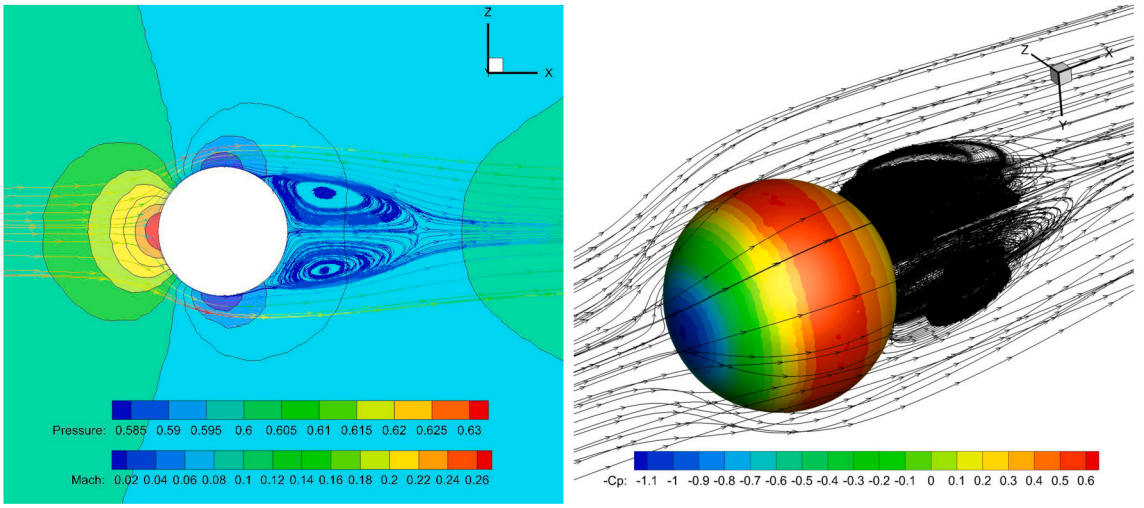

Fig. 14. Subsonic flow passing through a viscous sphere by the third-order compact GKS. Ma = 0.2535. Re = 118.

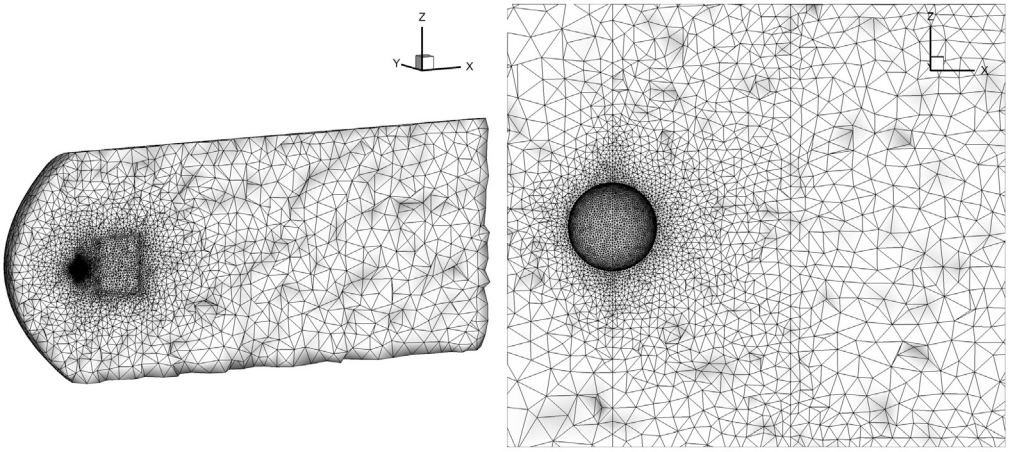

Fig. 15. Supersonic flow passing through a viscous sphere. Mesh number: 665,914.

Table 5
Quantitative comparisons between the current scheme and the reference solution for the supersonic viscous flow over a sphere.

Scheme	Grid Number	Cd	θ	L	Shock stand-off
WENO6 [17]	909,072	1.282	126.9	1.61	0.69
Current 3rd	665,914	1.274	126.3	1.64	0.66-0.82 (0.72)

based on the diameter $D = 1$. The Prandtl number is $Pr = 1$. The tetrahedral mesh with an upstream length of 5 and a downstream length of 40 is shown in Fig. 15. The first mesh size at the wall has a thickness $2.3 \times 10^{-2} D$. The numerical results obtained by the third-order compact GKS are shown in Fig. 16. Quantitative results are listed in Table 5, which have good agreement with those given by Nagata et al. [17]. Note that the proposed second-order GKS cannot survive for this case. The phenomenon that the second-order GKS is less robust than the third-order CGKS in the current study is probably due to the instability associated with the linear second-order least-square reconstruction as analyzed in [5].

5.6. Transonic inviscid flow around ONERA M6 wing

As a classic validation case for compressible external flow, the transonic flow over the ONERA M6 wing is tested. Experimental data are reported in [22], where the flow is fully turbulent. Same as the inviscid calculation in [14], an incoming Mach number Ma = 0.8395 and an angle of attack AOA = 3.06° are used, which correspond to a rough prediction of the flow field under a very high Reynolds number. In the computation, the wing has a slip wall boundary condition, and the Riemann invariants are applied 10

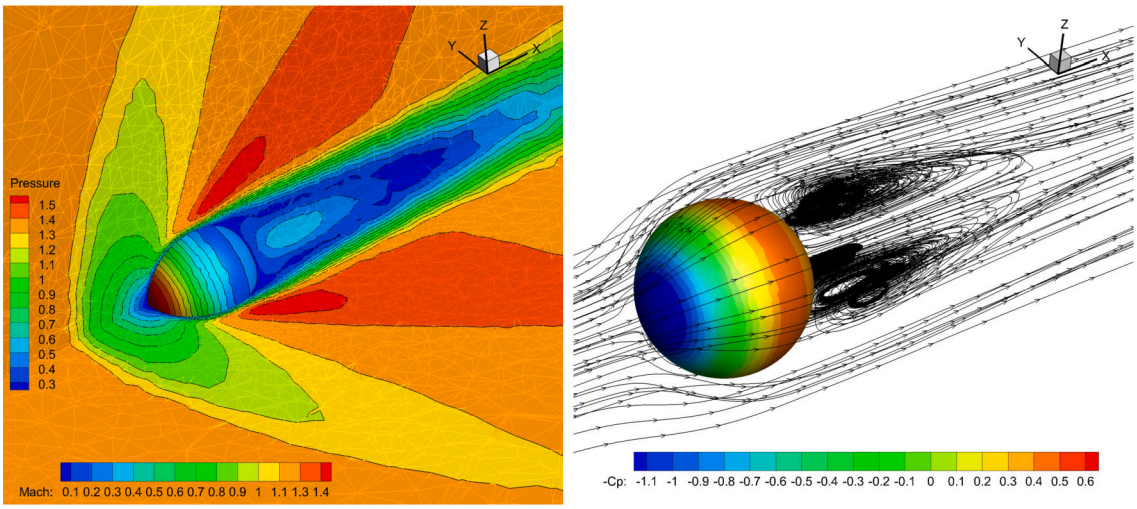

Fig. 16. Supersonic flow passing through a viscous sphere by the third-order compact GKS. Ma = 1.2. Re = 300.

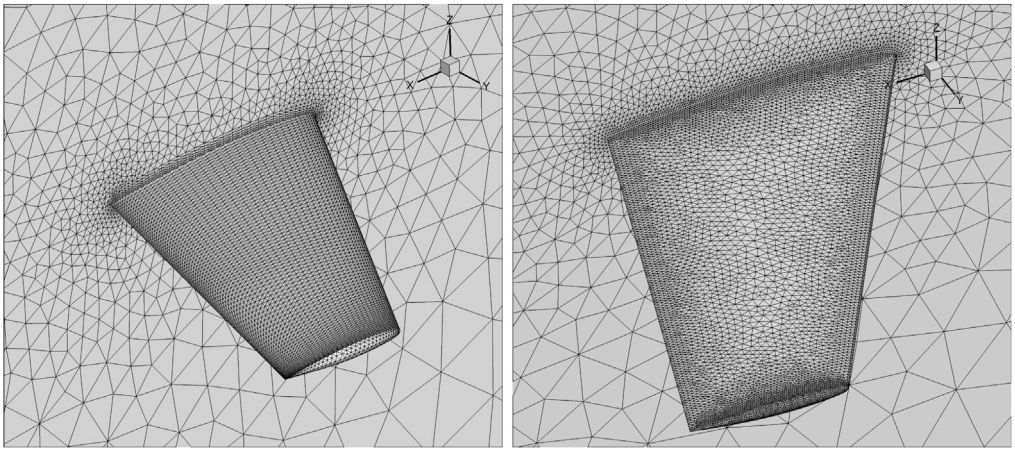

Fig. 17. Mesh for the inviscid ONERA M6 wing. Left: Mesh I with 294,216 cells. Right: Mesh II with 347,094 cells.

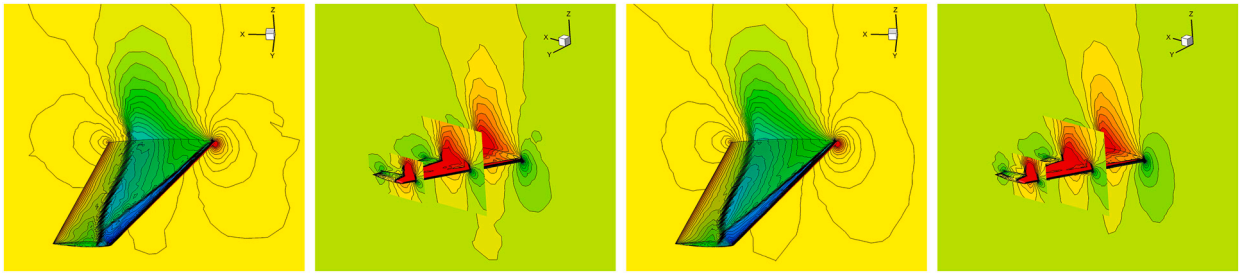

Fig. 18. Transonic flow over an inviscid ONERA M6 wing under Mesh I. Ma = 0.8935. AOA = 3.06°. Left: The second-order GKS. Right: The third-order GKS.

times of the root chord length away from the wing. Two sets of meshes are used to test the mesh sensitivity, as shown in Fig. 17. For each mesh, the results from the second and third-order GKS are presented. The surface pressure distributions and Mach number slices at different wing sections under Mesh I for both schemes are shown in Fig. 18. The "Lambda" shock is resolved from both schemes. Third-order scheme presents accurate solutions with high resolution in pressure and Mach contours in smooth region. Similar conclusions can be drawn from the results obtained from Mesh II, as shown in Fig. 20. Quantitatively comparisons on the pressure distributions at six different locations on the wing are given in Fig. 19 and Fig. 21. A better agreement in the secondary shock position is obtained with Mesh II at the semi-span locations Y/B = 0.20, 0.44, and 0.65.

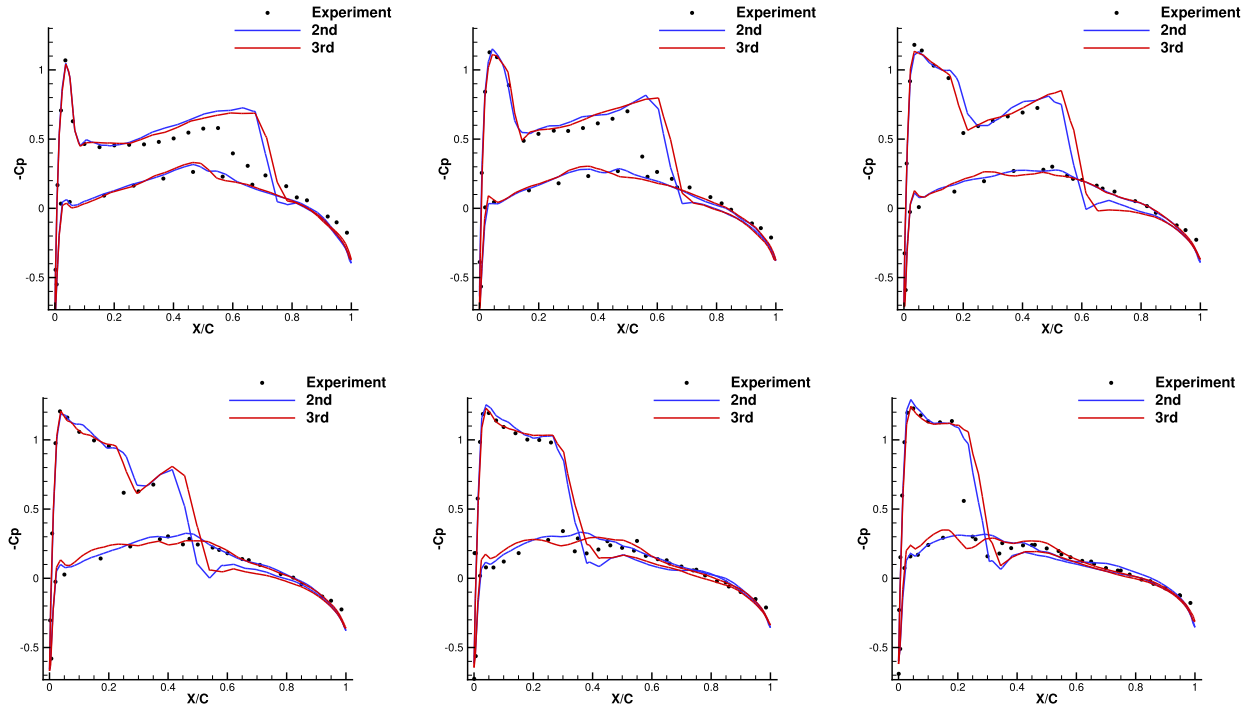

Fig. 19. Pressure distributions for wing section at different semi-span locations Y/B on the ONERA M6 wing under Mesh I. Ma = 0.8935. AOA = 3.06°. Top: Y/B = 0.20, 0.44, 0.65 from left to right. Bottom: Y/B = 0.80, 0.90, 0.95 from left to right.

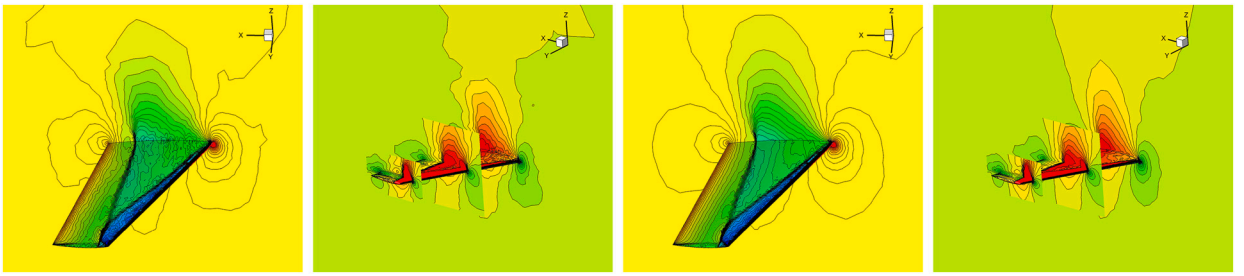

Fig. 20. Transonic flow over an inviscid ONERA M6 wing under Mesh II. Ma = 0.8935. AOA = 3.06°. Left: The second-order GKS. Right: The third-order GKS.

5.7. Supersonic flow over a YF-17 fighter

The inviscid supersonic flow passing through a complete aircraft model is computed. The computational mesh for a YF-17 ("Cobra") fighter model is shown in Fig. 22 which is provided at "https://cgns.github.io/CGNSFiles.html". A free stream at a Mach number Ma = 1.8 and an angle of attack AOA = 1.25 are adopted as the initial conditions. The surface pressure, Mach number distributions, and streamlines are presented in Fig. 23 for the GKS with the second-order WENO reconstruction. Complicated shocks appear in the locations including the nose, cockpit-canopy wing, horizontal stabilizer, and vertical stabilizer. A slightly smoother solution is obtained by the compact GKS with the third-order HWENO reconstruction, as shown in Fig. 24. The maximum Mach number on the surface is 2.4 for the second-order scheme and 2.28 for the third-order one. The current algorithm can handle complicated geometry, such as the mesh skewness near the wing tips and the lack of neighboring cell for the cell near boundary corners. The compact GKS demonstrates good mesh adaptability in the computation. The residuals for both cases cannot be reduced to a very small value, same as that in lots of WENO reconstruction-based schemes. This issue needs further investigation.

5.8. Hypersonic flow around a blunt body

A space-shuttle-like blunt-body model is considered to test the robustness of the schemes for the hypersonic inviscid flow. The initial condition has Ma = 5 and AOA = 0°. The surface mesh is given in Fig. 25, where the controlling points of the quadratic elements are shown. The pressure distributions are shown in Fig. 26, where no significant differences are observed in the results from the second-order and the third-order GKS. The Mach number distribution and streamlines are also plotted in Fig. 27.

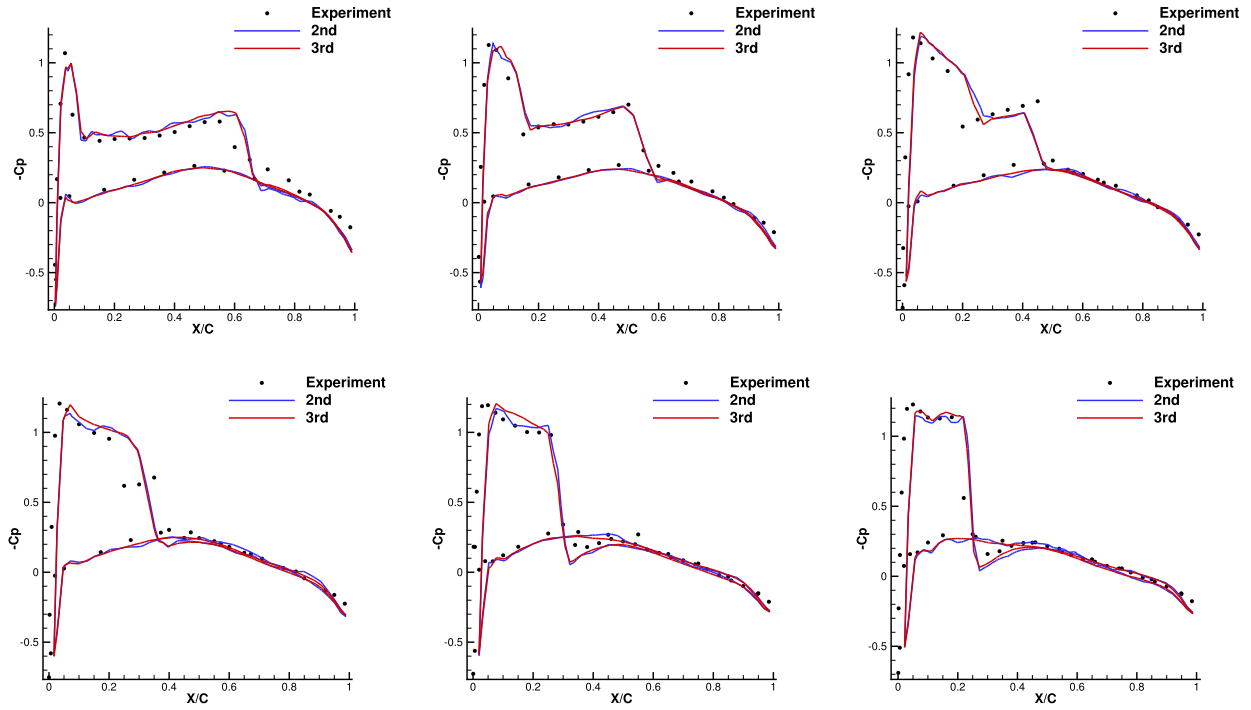

Fig. 21. Pressure distributions for wing section at different semi-span locations Y/B on the ONERA M6 wing under Mesh II. Ma = 0.8935. AOA = 3.06°. Top: Y/B = 0.20, 0.44, 0.65 from left to right. Bottom: Y/B = 0.80, 0.90, 0.95 from left to right.

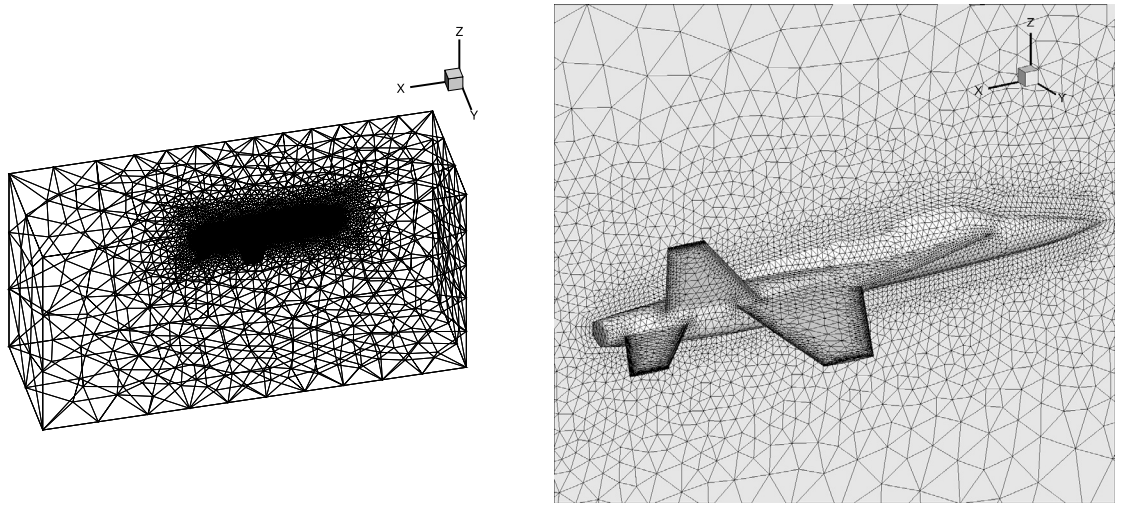

Fig. 22. Supersonic flow passing through a YF-17 ("Cobra") model. Ma = 1.8. AOA = 1.25. Mesh number: 325,096.

6. Conclusion

A third-order compact Gas-Kinetic Scheme (GKS) has been developed for the Euler and Navier-Stokes solution on three-dimensional tetrahedral meshes. One of the key innovations of this third-order compact GKS, compared to traditional Riemann-solver-based Finite Volume Methods (FVM), lies in its reliance on the time-dependent evolution solution of the gas distribution function. This function, evaluated at the Gaussian points of the cell interface, allows for precise calculation of both time-accurate conservative flow variables and their fluxes throughout the entire time step. Consequently, the cell-averaged conservative flow variables and their gradients within each control volume are updated via the time-integration of the interface flux transport and the surface integral of the conservative flow variables around the control volume boundaries (interfaces). With the cell-averaged flow variables and their gradients inside each control volume, a third-order spatial reconstruction can be attained through compact stencils utilizing only von Neumann neighbouring cells. In contrast, traditional third-order finite volume Weighted Essentially Non-Oscillatory (WENO)

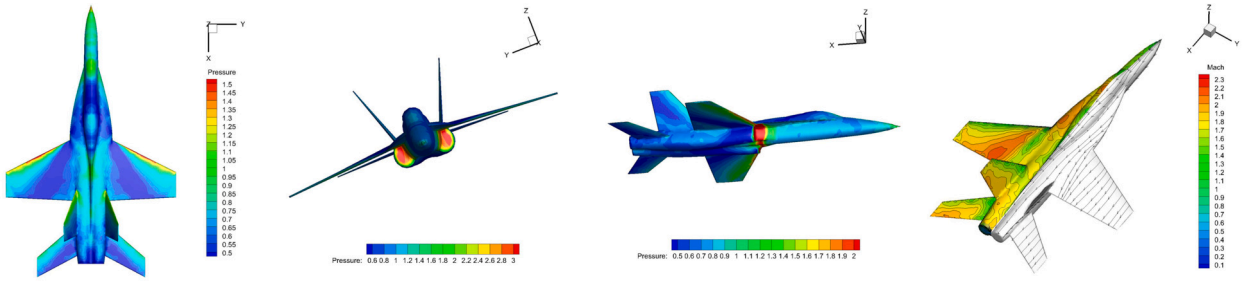

Fig. 23. Supersonic flow passing through a YF-17 ("Cobra") model by the second-order GKS. Ma = 1.8. AOA = 1.25°.

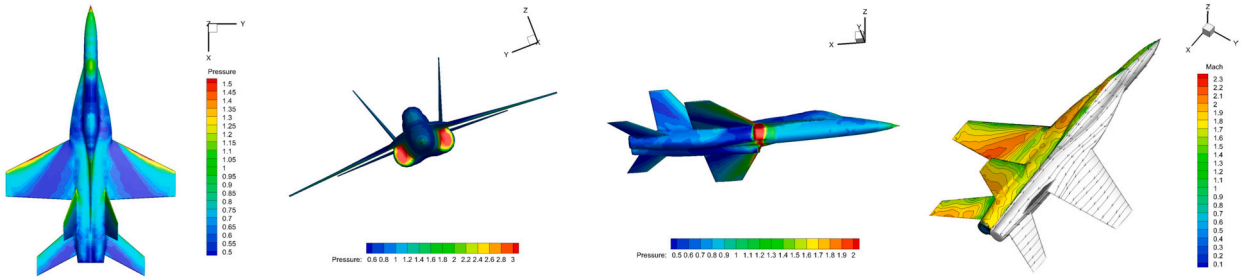

Fig. 24. Supersonic flow passing through YF-17 ("Cobra") model by the third-order GKS. Ma = 1.8. AOA = 1.25°.

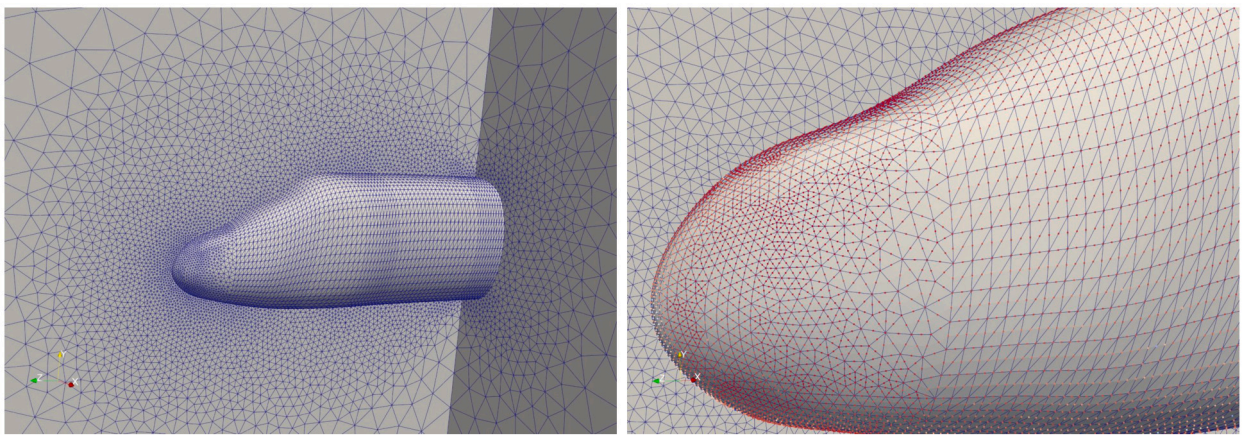

Fig. 25. Hypersonic inviscid flow over a blunt body. Mesh number: 117,221.

schemes, such as the one referenced in [39], necessitate the use of non-compact stencils that involve neighbouring-neighbour cells. The present third-order compact GKS outperforms traditional third-order finite volume WENO schemes in terms of parallelism and programming portability. This is due to the employment of the same data structure as the second-order finite volume method in terms of the reconstruction stencils.

High-order methods, particularly when transitioning from structured to unstructured tetrahedral meshes, can lead to linear instability. Even a second order FVM on a tetrahedral mesh may become linearly unstable when using a compact stencil with only von Neumann neighbouring cells. Similar instabilities are also associated with high-order methods based on Riemann solvers with a compact stencil. Moreover, traditional WENO strategies based on these compact stencils struggle to handle discontinuities. However, the compact third-order GKS, which directly evolves the cell-averaged first-order spatial derivatives of flow variables, has proven numerically the linear stability on tetrahedral mesh through smooth inviscid and viscous tests. To further enhance the mesh adaptability and robustness of the scheme, a new reconstruction based on two-step and multi-resolution WENO methods has been proposed. This also naturally yields a new second-order GKS as a byproduct, maintaining compactness in the reconstruction. The proposed reconstruction considers potential singularities resulting from mesh distortion or boundary corners and is well-suited for arbitrary meshes in engineering applications.

The compact GKS employs a two-stage time discretization to ensure temporal accuracy and demonstrates greater efficiency compared to third-order FVMs based on Runge-Kutta time stepping in hexahedral mesh [10]. The compact GKS exhibits robustness, high accuracy, and low dissipation. The reliable mesh adaptability is validated in the supersonic flow computation over a complete

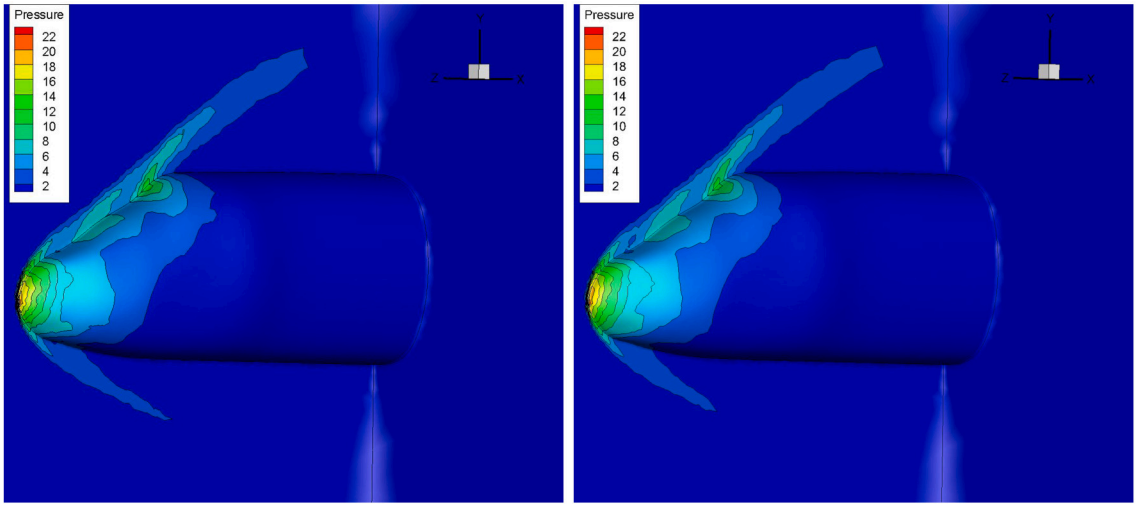

Fig. 26. Pressure distributions around the blunt body. Ma = 5.0. AOA = 0.0°. Left: the second-order GKS. Right: the third-order GKS.

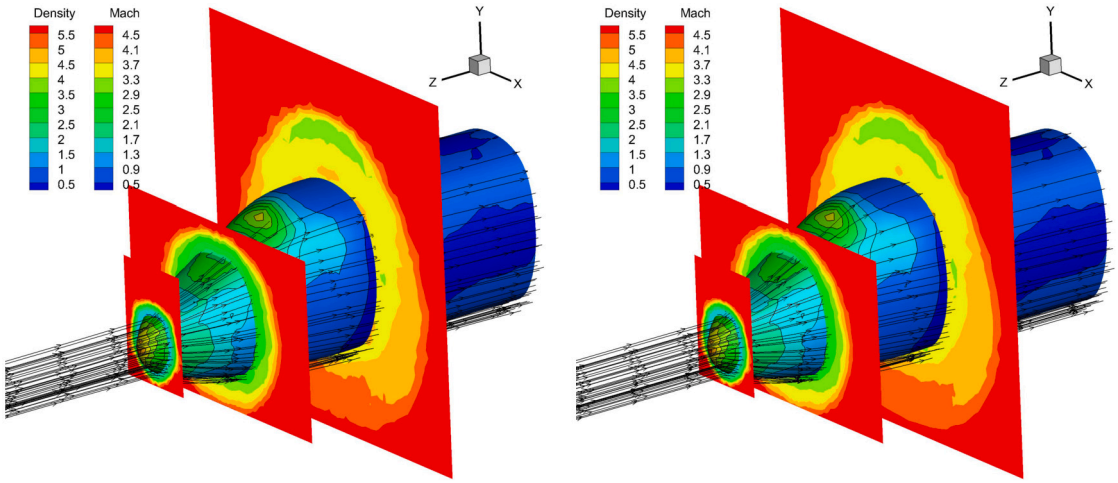

Fig. 27. Mach number distribution, stream-lines, and surface density distributions around the blunt body. Ma = 5.0. AOA = 0.0°. Left: the second-order GKS. Right: the third-order GKS.

aircraft model. A large explicit time step with a CFL number 1 can be used for most test cases. In summary, the proposed compact GKS, employing two-stage time discretization and two-step multi-resolution WENO reconstruction, displays excellent numerical performance among current compact schemes on a tetrahedral mesh. The compact GKS has also been developed for hybrid meshes with high aspect ratios in the boundary layer for supersonic and hypersonic viscous flow computations.

CRediT authorship contribution statement

Our group has been working on the topic for a long time. The research output is coming from our joint effort. All authors read and approved the final manuscript.

Declaration of competing interest

The authors declare that they have no known competing financial interests or personal relationships that could have appeared to influence the work reported in this paper.

Data availability

Data will be made available on request.

Acknowledgements

The authors would like to thank Dr. Jun Zhu for helpful discussion, and be grateful to Mr. Nianhua Wang, Dr. Yangyang Liu, and Dr. Liming Yang for providing computational meshes in some test cases. The current research is supported by National Natural Science Foundation of China (12172316, 12302378), CORE as a joint research centre for ocean research between QNLM and HKUST through the project QNLM20SC01-A and QNLM20SC01-E, and Hong Kong research grant council 16208021 and 16301222.

References

[1] Antonis F. Antoniadis, Panagiotis Tsoutsanis, Dimitris Drikakis, Assessment of high-order finite volume methods on unstructured meshes for rans solutions of aeronautical configurations, Comput. Fluids 146 (2017) 86–104.
[2] Prabhu Lal Bhatnagar, Eugene P. Gross, Max Krook, A model for collision processes in gases. I. Small amplitude processes in charged and neutral one-component systems, Phys. Rev. 94 (3) (1954) 511.
[3] Jian Cheng, Xiaodong Liu, Tiegang Liu, Hong Luo, A parallel, high-order direct discontinuous Galerkin method for the Navier-Stokes equations on 3d hybrid grids, Commun. Comput. Phys. 21 (5) (2017) 1231–1257.
[4] Michael Dumbser, Arbitrary high order PNPM schemes on unstructured meshes for the compressible Navier–Stokes equations, Comput. Fluids 39 (1) (2010) 60–76.
[5] F. Haider, J.-P. Croisille, B. Courbet, Stability analysis of the cell centered finite-volume MUSCL method on unstructured grids, Numer. Math. 113 (4) (2009) 555–600.
[6] Hung T. Huynh, A flux reconstruction approach to high-order schemes including discontinuous Galerkin methods, in: 18th AIAA Computational Fluid Dynamics Conference, 2007, p. 4079.
[7] Xing Ji, High-order non-compact and compact gas-kinetic schemes, PhD thesis, Hong Kong University of Science and Technology, 2019.
[8] Xing Ji, Kun Xu, Performance enhancement for high-order gas-kinetic scheme based on WENO-adaptive-order reconstruction, Commun. Comput. Phys. 28 (2) (2020) 539–590.
[9] Xing Ji, Fengxiang Zhao, Wei Shyy, Kun Xu, A HWENO reconstruction based high-order compact gas-kinetic scheme on unstructured mesh, J. Comput. Phys. (2020) 109367.
[10] Xing Ji, Fengxiang Zhao, Wei Shyy, Kun Xu, Compact high-order gas-kinetic scheme for three-dimensional flow simulations, AIAA J. 59 (8) (2021) 2979–2996.
[11] Zhe Ji, Tian Liang, Lin Fu, A class of new high-order finite-volume TENO schemes for hyperbolic conservation laws with unstructured meshes, J. Sci. Comput. 92 (2) (2022) 61.
[12] Jiequan Li, Zhifang Du, A two-stage fourth order time-accurate discretization for Lax–Wendroff type flow solvers I. Hyperbolic conservation laws, SIAM J. Sci. Comput. 38 (5) (2016) A3046–A3069.
[13] Wanai Li, Efficient Implementation of High-Order Accurate Numerical Methods on Unstructured Grids, Springer, Berlin, Heidelberg, 2014.
[14] Yangyang Liu, Liming Yang, Chang Shu, Huangwei Zhang, Three-dimensional high-order least square-based finite difference-finite volume method on unstructured grids, Phys. Fluids 32 (12) (2020) 123604.
[15] Hong Luo, Luqing Luo, Robert Nourgaliev, Vincent A. Mousseau, Nam Dinh, A reconstructed discontinuous Galerkin method for the compressible Navier–Stokes equations on arbitrary grids, J. Comput. Phys. 229 (19) (2010) 6961–6978.
[16] Dimitri Mavriplis, Revisiting the least-squares procedure for gradient reconstruction on unstructured meshes, in: 16th AIAA Computational Fluid Dynamics Conference, 2003, p. 3986.
[17] T. Nagata, T. Nonomura, S. Takahashi, Y. Mizuno, K. Fukuda, Investigation on subsonic to supersonic flow around a sphere at low Reynolds number of between 50 and 300 by direct numerical simulation, Phys. Fluids 28 (5) (2016) 056101.
[18] Jianhua Pan, Qian Wang, Yusi Zhang, Yuxin Ren, High-order compact finite volume methods on unstructured grids with adaptive mesh refinement for solving inviscid and viscous flows, Chin. J. Aeronaut. 31 (9) (2018) 1829–1841.
[19] Liang Pan, Kun Xu, Qibing Li, Jiequan Li, An efficient and accurate two-stage fourth-order gas-kinetic scheme for the Euler and Navier–Stokes equations, J. Comput. Phys. 326 (2016) 197–221.
[20] Ajay Prasad, Chin-Yuan Perng, Jeffrey Koseff, Some Observations on the Influence of Longitudinal Vortices in a Lid-Driven Cavity Flow, 1988, p. 3654.
[21] Ajay K. Prasad, Jeffrey R. Koseff, Reynolds number and end-wall effects on a lid-driven cavity flow, Phys. Fluids A, Fluid Dyn. 1 (2) (1989) 208–218.
[22] V. Schmitt, Pressure distributions on the ONERA M6-wing at transonic Mach numbers, experimental data base for computer program assessment, AGARD AR-138, 1979.
[23] David C. Seal, Yaman Güçlü, Andrew J. Christlieb, High-order multiderivative time integrators for hyperbolic conservation laws, J. Sci. Comput. 60 (1) (2014) 101–140.
[24] C. Shu, L. Wang, Y.T. Chew, Numerical computation of three-dimensional incompressible Navier–Stokes equations in primitive variable form by DQ method, Int. J. Numer. Methods Fluids 43 (4) (2003) 345–368.
[25] Chi-Wang Shu, High order WENO and DG methods for time-dependent convection-dominated PDEs: a brief survey of several recent developments, J. Comput. Phys. 316 (2016) 598–613.
[26] Chi-Wang Shu, Stanley Osher, Efficient implementation of essentially non-oscillatory shock-capturing schemes, II, in: Upwind and High-Resolution Schemes, Springer, 1989, pp. 328–374.
[27] Sadatoshi Taneda, Experimental investigation of the wake behind a sphere at low Reynolds numbers, J. Phys. Soc. Jpn. 11 (10) (1956) 1104–1108.
[28] Qian Wang, Compact High-Order Finite Volume Method on Unstructured Grids, PhD thesis, Tsinghua University, June 2017.
[29] Z.J. Wang, Y. Li, F. Jia, G.M. Laskowski, J. Kopriva, U. Paliath, R. Bhaskaran, Towards industrial large eddy simulation using the FR/CPR method, Comput. Fluids 156 (2017) 579–589.
[30] Paul Woodward, Phillip Colella, The numerical simulation of two-dimensional fluid flow with strong shocks, J. Comput. Phys. 54 (1) (1984) 115–173.
[31] Yidong Xia, Xiaodong Liu, Hong Luo, A finite volume method based on WENO reconstruction for compressible flows on hybrid grids, in: 52nd Aerospace Sciences Meeting, 2014, p. 0939.
[32] Kun Xu, A gas-kinetic BGK scheme for the Navier–Stokes equations and its connection with artificial dissipation and Godunov method, J. Comput. Phys. 171 (1) (2001) 289–335.
[33] Kun Xu, Direct Modeling for Computational Fluid Dynamics: Construction and Application of Unified Gas-Kinetic Schemes, World Scientific, 2014.
[34] Xiaoquan Yang, Jian Cheng, Hong Luo, Qijun Zhao, Robust implicit direct discontinuous Galerkin method for simulating the compressible turbulent flows, AIAA J. 57 (3) (2019) 1113–1132.
[35] Meilin Yu, Z.J. Wang, Yen Liu, On the accuracy and efficiency of discontinuous Galerkin, spectral difference and correction procedure via reconstruction methods, J. Comput. Phys. 259 (2014) 70–95.
[36] Fengxiang Zhao, Xing Ji, Wei Shyy, Kun Xu, A compact high-order gas-kinetic scheme on unstructured mesh for acoustic and shock wave computations, J. Comput. Phys. 449 (2022) 110812.

[37] Fengxiang Zhao, Xing Ji, Wei Shyy, Kun Xu, High-order compact gas-kinetic schemes for three-dimensional flow simulations on tetrahedral mesh, Adv. Aerodyn. 5 (1) (2023) 1–28.
[38] Zhong Zhao, Lei He, Xianyao He, Design of general CFD software PHengLEI (in Chinese), Comput. Eng. Sci. 42 (2) (2020) 210–219.
[39] Jun Zhu, Chi-Wang Shu, A new type of third-order finite volume multi-resolution WENO schemes on tetrahedral meshes, J. Comput. Phys. 406 (2020) 109212.